

Active galactic nuclei at $z \sim 1.5$ – II. Black hole mass estimation by means of broad emission lines

J. E. Mejía-Restrepo,^{1★} B. Trakhtenbrot,^{2†} P. Lira,¹ H. Netzer³ and D. M. Capellupo^{3,4}

¹Departamento de Astronomía, Universidad de Chile, Camino el Observatorio 1515, Santiago, Chile

²Institute for Astronomy, Department of Physics, ETH Zurich, Wolfgang-Pauli-Strasse 27, CH-8093 Zurich, Switzerland

³School of Physics and Astronomy, Tel Aviv University, Tel Aviv 69978, Israel

⁴Department of Physics, McGill University, Montreal, QC H3A 2T8, Canada

Accepted 2016 March 4. Received 2016 February 10; in original form 2015 November 17

ABSTRACT

This is the second in a series of papers aiming to test how the mass (M_{BH}), accretion rate (\dot{M}) and spin (a_*) of supermassive black holes (SMBHs) determine the observed properties of type I active galactic nuclei (AGN). Our project utilizes a sample of 39 unobscured AGN at $z \simeq 1.55$ observed by Very Large Telescope/X-Shooter, selected to map a large range in M_{BH} and L/L_{Edd} and covers the most prominent UV–optical (broad) emission lines, including $\text{H}\alpha$, $\text{H}\beta$, $\text{Mg II } \lambda 2798$ and $\text{C IV } \lambda 1549$. This paper focuses on single-epoch, ‘virial’ M_{BH} determinations from broad emission lines and examines the implications of different continuum modelling approaches in line width measurements. We find that using a *local* power-law continuum instead of a physically motivated thin disc continuum leads to only slight underestimation of the full width at half-maximum (FWHM) of the lines and the associated $M_{\text{BH}}(\text{FWHM})$. However, the line dispersion σ_{line} and associated $M_{\text{BH}}(\sigma_{\text{line}})$ are strongly affected by the continuum placement and provides less reliable mass estimates than FWHM-based methods. Our analysis shows that $\text{H}\alpha$, $\text{H}\beta$ and Mg II can be safely used for virial M_{BH} estimation. The C IV line, on the other hand, is not reliable in the majority of the cases; this may indicate that the gas emitting this line is not virialized. While $\text{H}\alpha$ and $\text{H}\beta$ show very similar line widths, the mean $\text{FWHM}(\text{Mg II})$ is about 30 per cent narrower than $\text{FWHM}(\text{H}\beta)$. We confirm several recent suggestions to improve the accuracy in C IV -based mass estimates, relying on other UV emission lines. Such improvements do not reduce the scatter between C IV -based and Balmer-line-based mass estimates.

Key words: galaxies: active – quasars: emission lines – quasars: general.

1 INTRODUCTION

The mass (M_{BH}) of supermassive black holes (SMBHs) along with the SMBH spin (a_*) and accretion rate (\dot{M}) are the fundamental parameters that drive the physical, geometric and kinematic properties of the SMBH environment (e.g. Kaspi et al. 2005; Slone & Netzer 2012; Capellupo et al. 2015). M_{BH} is also known to be correlated with several properties of the host galaxy, suggesting a so-called coevolutionary scenario for the SMBH and stellar component of the host (e.g. Ferrarese & Merritt 2000; Häring & Rix 2004; Gültekin et al. 2009; Xiao et al. 2011). Therefore, accurate and precise determinations of M_{BH} , across cosmic epochs, are crucial for our understanding of SMBH physics and evolution.

For unobscured, type I actively growing SMBHs (active galactic nuclei – AGN), M_{BH} can be estimated from single-epoch spectra of

several broad emission lines. The method, which was used for many large samples of AGN across cosmic epochs (e.g. Croom et al. 2004; McLure & Dunlop 2004; Onken et al. 2004; Fine et al. 2006; Shen et al. 2008; Rafiee & Hall 2011; Trakhtenbrot & Netzer 2012), is based on a combination of two basic ingredients (Vestergaard 2002; Peterson et al. 2004). First, reverberation mapping (RM) experiments provide an empirical relation between the broad line region (BLR) size and the AGN continuum luminosity ($R_{\text{BLR}} = K'(\lambda L_\lambda)^\alpha$, with $\alpha \sim 0.5$ – 0.7 ; see Kaspi et al. 2000, 2005; Bentz et al. 2009, 2013, and references therein). Secondly, the gas in the BLR is assumed to be virialized (as suggested by several empirical studies, e.g. Peterson & Wandel 1999; Onken et al. 2004). After taking the line width of the BLR lines as a natural estimation of the virial velocity of the gas in the BLR (V_{BLR}), one may obtain the mass from the virial relation:

$$M_{\text{BH}} = f G^{-1} R_{\text{BLR}} V_{\text{BLR}}^2 = K(\lambda L_\lambda)^\alpha \text{FWHM}^2, \quad (1)$$

* E-mail: jemejia@das.uchile.cl

† Zwicky postdoctoral fellow.

where $K = K'G^{-1}f$ and f is a general geometrical function which corrects for the unknown structure and inclination to the line of sight. f can be determined experimentally by requiring $RM-M_{BH}$ estimations to be consistent, on average, with those predicted from the M_{BH} -bulge stellar velocity dispersion ($M_{BH}-\sigma_*$) relation of local galaxies where M_{BH} have been dynamically estimated (e.g. Onken et al. 2004; Woo et al. 2010, 2015; Graham et al. 2011; Graham 2016). In this paper, we assume $f = 1$, which is appropriate for the full width at half-maximum (FWHM) $M_{BH}(H\beta)$ estimates (Woo et al. 2015). However, in addition to the still large uncertainty in this value (50 per cent), f can also be different for different lines and could even depend on luminosity and/or line properties (e.g. equivalent widths, line offsets, FWHM; Shen 2013).

Among the RM-based $R_{BLR}-L$ relations, the most reliable one is the $R_{BLR}(H\beta)-L_{5100}$ relation, which is the only one based on a large number of sources, with $L_{5100} \lesssim 10^{46}$ erg s $^{-1}$. Thus, the M_{BH} determination based on other lines and luminosities at other wavelengths needs to be re-calibrated to match M_{BH} measurements based on $H\beta$ and L_{5100} . Particularly, C IV $\lambda 1549$, hereafter C IV (e.g. Vestergaard & Peterson 2006; Park et al. 2013), Mg II $\lambda 2798$, hereafter Mg II (e.g. McLure & Jarvis 2002; Vestergaard & Osmer 2009; Wang et al. 2009; Trakhtenbrot et al. 2011; Shen & Liu 2012; Trakhtenbrot & Netzer 2012) and H α (e.g. Greene & Ho 2005; Xiao et al. 2011; Shen & Liu 2012) have been re-calibrated accordingly, and are widely used lines to determine M_{BH} at high redshifts.

Earlier M_{BH} re-calibrations based on Mg II and H α have showed good agreement and low scatter with $H\beta$ -based M_{BH} calibration (Greene & Ho 2005; Xiao et al. 2011; Trakhtenbrot & Netzer 2012). However, M_{BH} re-calibrations using the C IV line are more problematic, compared with those based on lower ionization lines. First, the correlation between the widths of C IV and the other lines was shown to be weak, or indeed insignificant, and to present a large scatter, in many AGN samples (e.g. Baskin & Laor 2005; Netzer et al. 2007; Shang et al. 2007; Shen et al. 2008; Fine et al. 2010; Ho et al. 2012; Shen & Liu 2012; Tilton & Shull 2013). Moreover, about 40 per cent of the objects have $FWHM(C IV) \lesssim FWHM(H\beta)$, in contrast to the expectations from RM experiments and the virial assumption, that suggest $FWHM(C IV) \simeq 2 \times FWHM(H\beta)$ (see detailed discussion in TN12, and additional samples in Ho et al. 2012, Shen & Liu 2012 and Tilton & Shull 2013). Secondly, significant blueshifts of the *entire* C IV profile (i.e. not necessarily a specific subcomponent of the line), reaching several thousand km s $^{-1}$, are ubiquitously measured in the vast majority of AGN (Richards et al. 2002, 2011; Baskin & Laor 2005; Shang et al. 2007; Trakhtenbrot & Netzer 2012). Some of these findings were explained either by a disc outflow wind (e.g. Gaskell 1982; Sulentic et al. 2007; Richards et al. 2011) or, alternatively, by scattering off an in-falling medium in the innermost C IV-emitting regions, which would produce the C IV blueshifts (e.g. Kallman & Krolik 1986; Goosmann & Gaskell 2007; Gaskell 2009; Gaskell & Goosmann 2013). Finally, the detailed re-analysis of the RM data for C IV performed by Denney (2012) found that the (narrowest) core of the broad C IV line does not reverberate in response to continuum variability. This implies that the *outermost* C IV-emitting regions may not be virialized, either. All this leads to the conclusion that the simplified models and prescriptions discussed above may be incorrect, or at least incomplete, for some lines.

The M_{BH} determination is also subjected to several uncertainties, related to the limitations of spectral analysis, and/or the need to make several assumptions regarding the universality of some AGN properties. The former includes the blending of neighbouring emission and/or absorption features, incorrect determination of the continuum emission (Shang et al. 2007, hereafter S07), poor statis-

tics due to non-homogeneous or small nature of the sample under study (e.g. Ho et al. 2012), poor data quality (e.g. Denney et al. 2013; Tilton & Shull 2013) and measurements obtained from non-simultaneous data (see e.g. Shen & Liu 2012; Marziani et al. 2013a). The latter, somewhat more fundamental uncertainties, include non-virial gas motion, the orientation of the (generally non-spherical) BLR with respect to the line of sight (Runnoe et al. 2014; Shen & Ho 2014; Brotherton, Singh & Runnoe 2015) and the extrapolation of the $R_{BLR}-L$ relations to luminosities which are well beyond the range probed by RM experiments.

There have been many efforts to improve single-epoch M_{BH} determinations, addressing some of the aforementioned limitations (e.g. Greene & Ho 2005; Vestergaard & Peterson 2006; Fine et al. 2008, 2010; Wang et al. 2009; Xiao et al. 2011; Shen & Liu 2012; Trakhtenbrot & Netzer 2012; Marziani et al. 2013a; Park et al. 2013; Runnoe et al. 2013; Brotherton et al. 2015; Zuo et al. 2015). Trakhtenbrot & Netzer (2012, hereafter TN12) combined Sloan Digital Sky Survey archival data (SDSS; Abazajian et al. 2009) with smaller surveys and samples to improve earlier Mg II-based M_{BH} prescriptions (e.g. McLure & Jarvis 2002; McLure & Dunlop 2004; Wang et al. 2009), by assuming virialization of the Mg II-emitting clouds. As mentioned above, the TN12 study emphasized the fact that a large fraction of AGN show $FWHM(C IV) < FWHM(H\beta)$. Marziani et al. (2013a, hereafter M13) also used SDSS data to perform an eigenvector 1 analysis (Boroson & Green 1992), and to separate the population into ‘population A’ ($FWHM(H\beta) < 4000$ km s $^{-1}$) and ‘population B’ ($FWHM(H\beta) > 4000$ km s $^{-1}$) sources. They suggested that $H\beta$ - and Mg II-based M_{BH} estimates in population B sources could be systematically overestimated due to a redshifted, extremely broad emission component. The study of Shen & Liu (2012) combined SDSS optical observations of high- z objects ($1.5 \lesssim z \lesssim 2.2$) with follow-up Folded-port InfraRed Echelle observations, which allowed them to compare and re-calibrate the C IV, Mg II, $H\beta$ and H α M_{BH} relations as well as contrast them with previous calibrations. While they found that $FWHM(Mg II)$ correlates well with the Balmer lines, the $FWHM(C IV)$ does not show such correlations and is not a reliable viral mass estimator. The Shen & Liu (2012) results are however subjected to low-quality SDSS data, non-homogeneous sample selection and non-simultaneous observations. Ho et al. (2012) obtained simultaneous UV, optical and infrared X-Shooter spectra for seven objects at $1.3 \lesssim z \lesssim 1.6$, resulting in similar conclusions regarding the usability of Mg II-based M_{BH} estimates, and the limitations associated with C IV.

The studies of Denney et al. (2013, hereafter D13) and Tilton & Shull (2013) claimed that in spectra of limited signal-to-noise ratio (S/N) and/or spectral resolution, $FWHM(C IV)$ measurements are underestimating the ‘real’ line widths, in objects with strong intrinsic absorption features that cannot be deblended from the emission lines. This would partially explain the TN12 finding that about 40 per cent of the objects show $FWHM(C IV) < FWHM(H\beta)$. However, objects with no evidence of absorption features, and yet ‘intrinsic’ line widths with $FWHM(C IV) < FWHM(H\beta)$ are known to exist (e.g. Corbin & Boroson 1996). After correcting for intrinsic C IV absorption, D13 claimed that although $FWHM(C IV)$ still does not correlate well with $FWHM(H\beta)$, $\sigma(C IV)$ shows a strong correlation with $\sigma(H\beta)$ and can safely be used for C IV-based M_{BH} determinations. Based on these results, Park et al. (2013) obtained high-quality data in 39 out of 45 objects of the RM experiments campaign and improved the Vestergaard & Peterson (2006) C IV-based M_{BH} estimator based on the $\sigma(C IV)$. Both D13 and Park et al. (2013) used non-homogeneous and multi-epoch samples that could affect their results. In addition, σ_{line} measurements are highly

dependent on the continuum determination method (see discussion in Peterson et al. 2004).

Recently, Runnoe et al. (2013, hereafter R13) and Brotherton et al. (2015) used a sample of 85 low-redshift ($0.03 < z < 1.4$) and low-luminosity ($43.37 < \log L_{5100} < 46.45$) AGN with quasi-simultaneous UV and optical spectra to propose a method to rehabilitate C IV for M_{BH} determination, based on a correlation that they found between the Si IV+O IV]–C IV line peak intensity ratio and the $\text{H}\beta$ –C IV FWHM ratio. This allowed these authors to predict $\text{FWHM}(\text{H}\beta)$ from measurements of the Si IV+O IV] emission. These studies suggested that this correlation may be driven by the so-called eigenvector 1.

In this work, we use X-Shooter high-quality observations that combines simultaneous UV, optical and infrared spectroscopy of a unique sample of AGN at $z \sim 1.55$, selected by both their M_{BH} and Eddington ratio, L/L_{Edd} as described in Capellupo et al. (2015, hereafter Paper I). Selecting objects at this redshift allows simultaneous observations of $\text{H}\alpha$, $\text{H}\beta$, Mg II and C IV, which is optimal for comparing the various mass determination methods. In Paper I, we showed that the accretion disc (AD) continuum of most of the objects (25 out of 30) can be successfully modelled by a geometrically thin, optically thick Shakura–Sunyaev AD (Shakura & Sunyaev 1973, hereafter SS73). The models were taken from Slone & Netzer (2012) who include several improvements upon the SS73 model, such as general relativity effects and a detailed treatment of the Comptonization in the disc atmosphere. Paper I shows that most earlier attempts to fit AD spectra to AGN failed because of the limited wavelength coverage and/or non-simultaneous observations. The continuation of this work, which includes nine more sources and a more comprehensive analysis, is described in Capellupo et al. 2016 (hereafter Paper III), which is published in this volume.

The purpose of this paper is to evaluate BH mass measurements based on different emission lines, as derived from our unique sample of X-Shooter spectra. We also aim to provide to the community M_{BH} correction factors that do not depend on the exact shape of the underlying continuum. The paper is structured as follows. In Section 2, we describe the sample. In Section 3, we first introduce the *local* and *global* thin disc continuum approaches and describe the fitting procedures we follow to model the continuum, emission lines, iron pseudo-continuum and Balmer continuum (BC). In Section 4, we present and discuss the main results, and in Section 5, we list the main conclusions of our work. Throughout this paper we assume a flat Λ cold dark matter cosmology with the following values for the cosmological parameters: $\Omega_{\Lambda} = 0.7$, $\Omega_{\text{M}} = 0.3$ and $H_0 = 70 \text{ km s}^{-1} \text{ Mpc}^{-1}$.

2 SAMPLE, DATA AND ANALYSIS

The analysis presented in this paper is based on a sample of luminous, type I AGN in a narrow redshift range around $z \simeq 1.55$, for which we have obtained high S/N single-epoch spectroscopic observations using the X-Shooter instrument on the Very Large Telescope. The 39 sources span a range in brightness of $i_{\text{AB}} \sim 16.8$ –20.9. The sample selection, data acquisition and reduction for the 30 brightest sources were described in detail in Paper I, and information about 9 other sources, obtained in ESO programme 092.B-0613, is provided in Paper III. Here, we only briefly highlight a few essential aspects.

The sample has been selected from the seventh data release of the SDSS (Abazajian et al. 2009) to homogeneously map the parameter space of M_{BH} and L/L_{Edd} . For the purposes of target selection, these quantities were initially obtained by spectral fitting of the

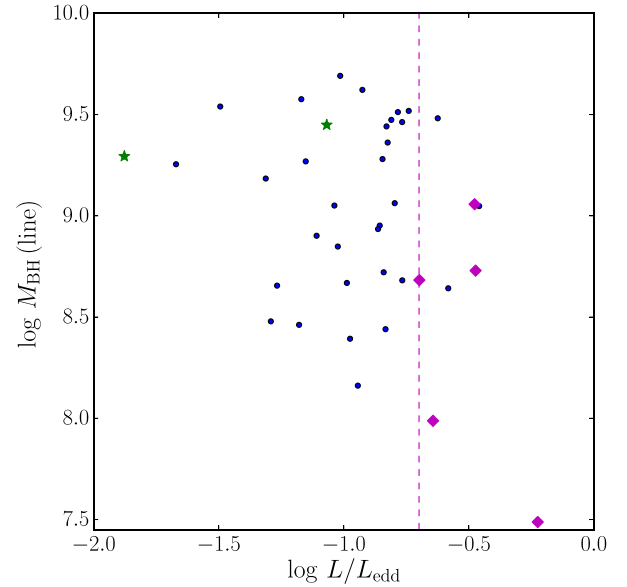


Figure 1. M_{BH} versus L/L_{Edd} using the values we obtained in this paper. Green stars and magenta diamonds represent the broad absorption line quasars (BALQSO) and the broad-Mg II, respectively (as defined in Section 4.3.4). The magenta dashed vertical line represents $L/L_{\text{Edd}}=0.2$.

Mg II broad emission line in the SDSS spectra as part of the large compilation described in TN12. In Fig. 1, we show M_{BH} versus L/L_{Edd} using updated values calculated in this paper based on the $\text{H}\alpha$ broad emission line and following the procedure that we describe in Section 4.4.

At the chosen redshift range of the sample, X-Shooter covers the rest-frame wavelength from about 1200 to 9200 Å. This broad spectral coverage has allowed us, after correction for Galactic extinction, to successfully model and constrain the observed spectral energy distributions (SEDs). As shown in Papers I and III, we obtain satisfactory thin AD model fits to 37 sources, 6 of which require an intrinsic reddening correction for a satisfactory fit. The wide wavelength coverage, together with the homogeneous selection of the sample in the $M_{\text{BH}}-L/L_{\text{Edd}}$ plane, enables us to test the performance of the single-epoch black hole mass estimators for the $\text{H}\alpha$, $\text{H}\beta$, Mg II and C IV lines and estimates the systemic bias induced when the physical SED is unknown.

In Fig. 2, we show the S/N for our X-Shooter spectra, measured at the peaks of each of the main emission lines under study, as well as at the corresponding continuum bands, as a function of i_{AB} . We note that, even in the spectral region which overlaps with the available SDSS spectra, the X-Shooter data provide a significant improvement in terms of S/N and spectral resolution (see an example in Fig. A1, described in Appendix A). All the sources have fairly high S/N ($\gtrsim 20$) at the peaks of the Mg II and C IV lines and the adjacent continuum bands. However, this is not the case for $\text{H}\alpha$ and $\text{H}\beta$. The continuum bands adjacent to $\text{H}\alpha$ are much noisier. Most of the objects have $\text{S/N} < 20$, and for those with $i_{\text{AB}} > 18.5$, the ratio is below 10. Nevertheless, we are able to obtain reliable $\text{H}\alpha$ line measurement because most objects have fairly high S/N at their $\text{H}\alpha$ line peak (34 out of 39 object have $\text{S/N} \gtrsim 20$ and all of them have $\text{S/N} \gtrsim 8$). Moreover, the relevant continuum bands around $\text{H}\alpha$ have low levels of contamination from iron or other, unresolved spectral features. Consequently, even a moderate continuum S/N (i.e. $\gtrsim 3$) is enough to have reliable $\text{H}\alpha$ fits. There are

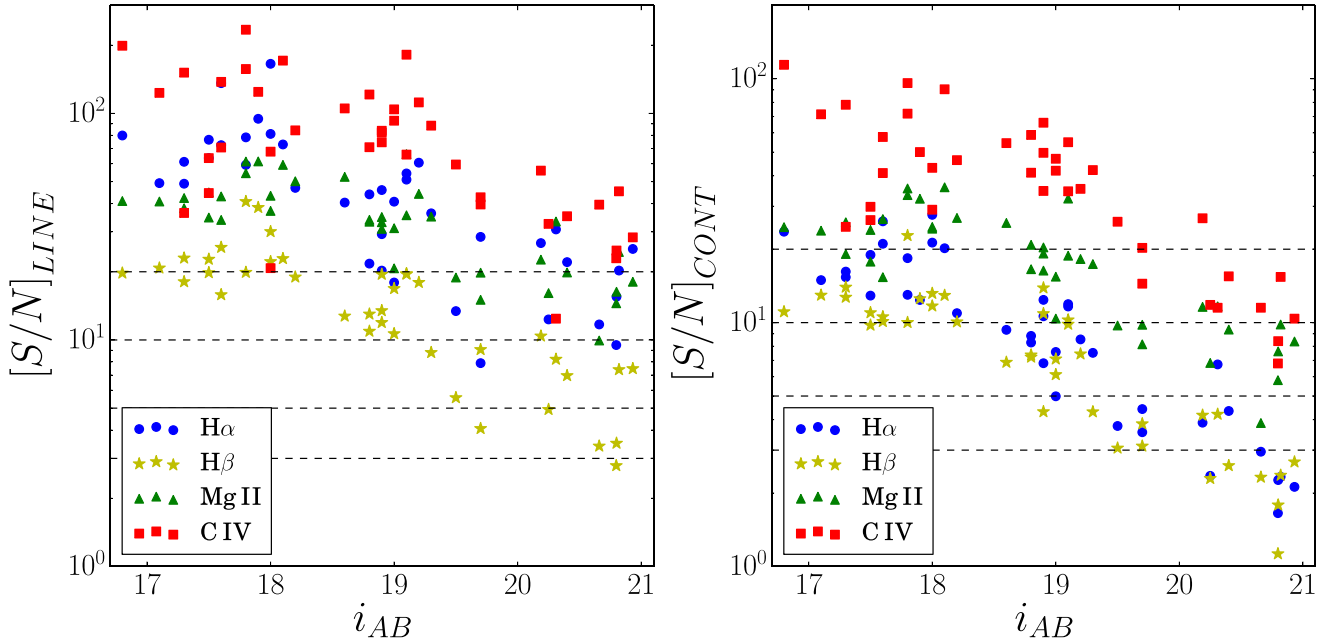


Figure 2. Signal-to-noise ratios (S/N) measured at the peaks of each of the main broad emission lines (left), and over the corresponding nearby continuum bands (right), plotted against optical brightness, i_{AB} . The black dashed lines represent, from bottom top, S/N equal to 3, 5, 10 and 20.

however four objects where $S/N < 3$ and their line measurements, especially their FWHM($H\alpha$) are somewhat uncertain.

Unfortunately, the $H\beta$ line measurements are more problematic. In addition to the fact that $H\beta$ is the weakest of the lines of interest, we can also see from Fig. 2 that the relevant continuum band in 21 out of 39 objects have $S/N \lesssim 10$, and 14 of them are actually below $S/N \sim 5$. Near-infrared (NIR) telluric absorption is another issue that could also crucially affect $H\beta$ line measurements. The spectral regions with known low atmospheric transmission in the NIR, between 13 000 to 15 000 Å typically translate to rest-frame bands at 4200–4500 Å and 5300–5800 Å at the redshift of the sample. These bands are known to show strong iron emission which are suppressed by such telluric absorption (see the example spectrum in Fig. 3 around 4400 and 5500 Å). The combined effect of the telluric absorption and the limited S/N achieved for the fainter sources severely affects the correct modelling of their iron emission around $H\beta$. This, in turn, significantly increases the measurement uncertainties related to $H\beta$, ultimately making $H\beta$ measurements of faint objects less reliable.

Fortunately, the $H\alpha$ line shows very similar profiles to $H\beta$ (e.g. Greene & Ho 2005) which is in accordance with the expected radial ionization stratification of the BLR (Kaspi et al. 2000). On the basis of these results, we can probe several aspects related to the $H\beta$ line using the more reliable $H\alpha$ measurements.

3 SPECTRAL DECOMPOSITION

In this section, we describe the analysis procedures we used to model the X-Shooter spectra and to obtain continuum and line emission measurements. We discuss separately the analysis of emission corresponding to the continuum, the blended iron features, and the emission line components. All the spectral modelling is done by employing the Levenberg–Marquardt algorithm for χ^2 minimization, using the PYTHON-based spectroscopic analysis package PYSPECKIT (Ginsburg & Mirocha 2011). The fitting is performed in the rest frame, after shifting the spectra using the improved SDSS redshifts

provided by Hewett & Wild (2010). We chose to use these redshifts, instead of using the O III] λ 5007 line observed within the X-Shooter data, because of the limited quality of the relevant data and modelling of the $H\beta$ –O III] λ 5007 spectral region (see Section 2) and the weak or absent O III] λ 5007 emission in many of our sources.

3.1 Continuum emission

We adopt here two different approaches to account for the continuum emission of the AGN, which we refer to as the *local* and *global* (thin disc) continuum approaches. The *local* continuum attempts to account for the usual approximation of the continuum emission by a single power law when the observed spectrum is limited to a narrow wavelength range. The *global* thin disc continuum, on the other hand, corresponds to the more physically motivated AD model that was obtained through a Bayesian analysis taking advantage of our wide spectral wavelength coverage (see Paper I). A comparison of the measurements obtained with both approaches will allow us to quantify the possible bias imposed by ignoring the real SED shape, when wide-enough wavelength coverage is not available.

3.1.1 Local continuum approach and biases

The *local* continuum approach consists of separately fitting the continuum emission surrounding each of the lines of interest. For every source in the sample, each of these continua is approximated by a single power law, which connects neighbouring spectral windows known to have little line contamination. Our specific choice of such line-free continuum bands rely on several similar works (S07; TN12), and are listed in Table 1.

The most important bias in the *local* approach is that it commonly uses non-real continuum windows that are affected by either (1) weak line emission flux such as the continuum window at 1700 Å that is used for C IV line fitting, (2) iron continuum emission that affects continuum windows around 2600 and 3000 Å, as well as those around 4650 and 5100 Å that are, respectively, used for Mg II

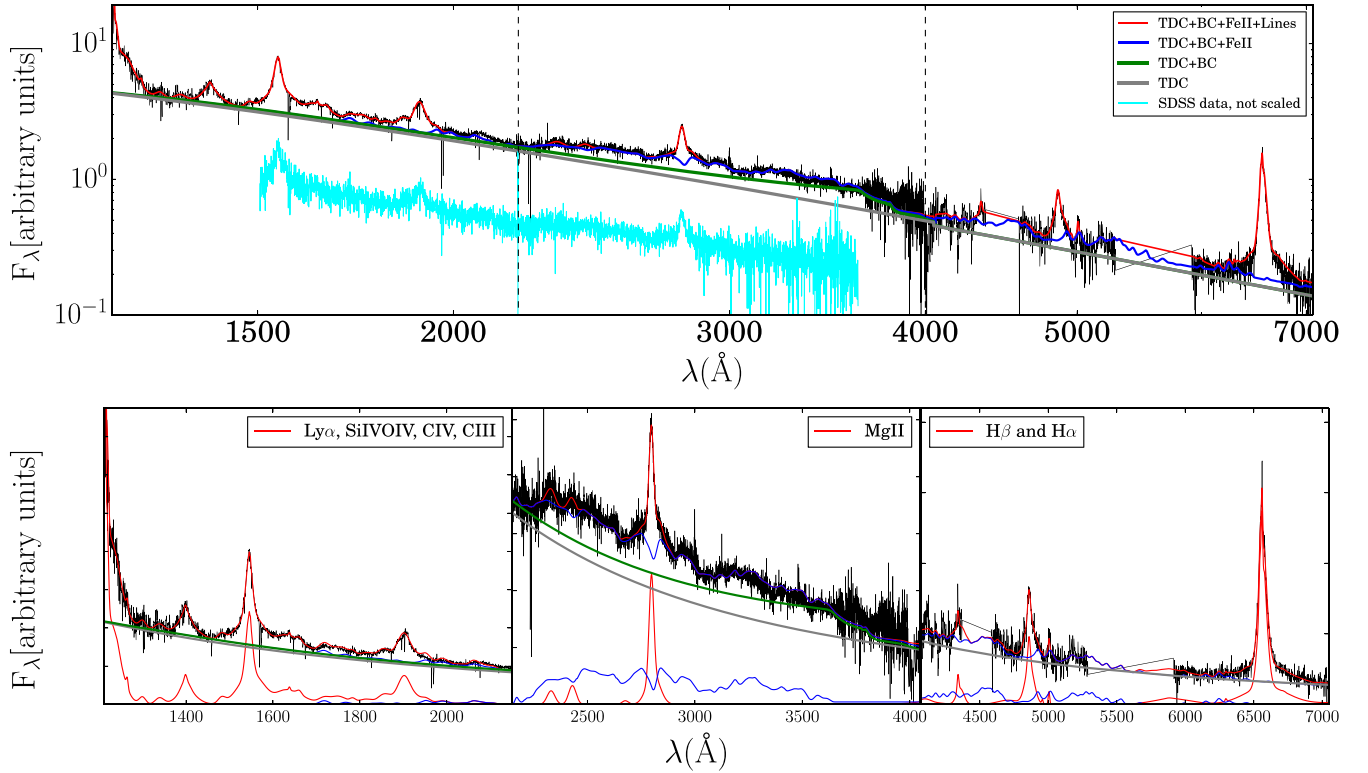


Figure 3. The rest-frame X-Shooter spectrum (top) and main emission line complexes (bottom), over the three X-Shooter bands (UV: left, optical: middle, infrared: right), for the source J0143–0056 and the corresponding line fitting using the *global* thin disc continuum approach. The observed spectrum is shown in black. The best-fitting continuum is shown in grey. The blue lines represent the additional best-fitting iron emission. The red lines represent the additional best-fitting models for the emission lines. For the sake of comparison, we show the SDSS of the source in cyan.

Table 1. Spectral pseudo-continuum windows used for our line fitting procedure under the *local* continuum approach. ^aFor each object, we manually adjusted the continuum bands, using the listed wavelength ranges as a reference.

Line complex	Continuum windows ^a	
Si IV+O IV]	1340–1360 Å	1420–1460 Å
C IV	1420–1460 Å	1680–1720 Å
C III]	1680–1720 Å	1960–2020 Å
Mg II	2650–2670 Å	3030–3070 Å
Hβ	4670–4730 Å	5080–5120 Å
Hα	6150–6250 Å	6950–7150 Å

and Hβ line fitting and finally, (3) the BC emission, at $\lambda < 3647$ Å, which can significantly affect Mg II measurements, and to a lesser extent even C IV measurements. All these biases are in the direction of an overestimation of the continuum emission when the *local* approach is used which will translate into FWHM and line flux underestimation.

An additional bias comes from the shape of the SED, particularly at the turn-over of most spectra at around 1000–1500 Å (exact wavelengths depend on BH mass, spin and accretion rate, see Papers I and III). The simple power-law approximation to the SED does not remain valid over this range and may lead to measurement biases of the line profile properties of C IV and Si IV+O IV] ($\lambda 1400$ (hereafter Si IV+O IV]). In this paper, we use our AD SED fittings to quantify these biases.

3.1.2 Thin disc continuum approach

The *global* AD approach is based on the best fits from the thin-AD continuum models obtained for each of the sources in Papers I and III. For the analysis in this paper, we do not consider the two objects with no satisfactory fits to the thin disc continuum model.

As explained in Papers I and III, the SEDs of the AD models used in this work are determined by M_{BH} , the accretion rate (\dot{M}), the spin (a_*) and the inclination of the disc with respect to the line of sight (θ).

We adopted a Bayesian procedure to fit the thin AD model spectra to the observed X-Shooter SEDs. M_{BH} and \dot{M} were taken as priors with Gaussian distributions centred on the observed values, obtained from Hα and L_{6200} measurements (following the procedures described in this paper), and with standard deviations of 0.3 and 0.2 dex, respectively.

Within the *global* continuum approach, we also consider the BC emission that peaks near the Balmer edge (3647 Å) and gradually decreases towards shorter wavelengths. The BC model we used is based on calculations of the photoionization code ION (Netzer 2006) with an H-atom containing 40 levels, solar abundances, hydrogen density of 10^{10} cm^{-3} , column density of 10^{23} cm^{-2} and ionization parameter of $10^{-1.5}$. The exact shape is insensitive to the exact value of these parameters, and the normalization is done by direct fits to the observations.

An additional contribution to the continuum emission is due to starlight, mostly at wavelengths longer than about 6000 Å. For our AGN sample such a contribution is marginal in 32 out of 39 objects and does not severely affect the continuum level and shape of the AGN SED as discussed in Papers I and III (<3 per cent at 6200 Å).

For the seven fainter objects we used the method described in Paper III which assumes a template from an 11-Gyr-old stellar population to model the host galaxy emission. The scale factor of the template is determined from the ratio of the measured EW($H\alpha$) and the median value of the EW($H\alpha$) distribution of the 29 brightest objects, as discussed in Paper III. The host galaxy contribution is subtracted before the thin disc continuum fitting for those objects which require this correction. We find that in this subsample the host galaxy contribution is between 6 per cent and 50 per cent at 6200 Å and smaller than 3 per cent at 3000 Å. We also tested several stellar populations in the age range from 1 to 11 Gyr, but we find no significant changes in the corrected spectrum (see Paper III for details).

Finally, combining the X-Shooter spectra obtained by three different arms (UV, Optical and NIR) may introduce additional uncertainties. As explained in Paper I, in most cases, the overlap and connection between the VIS and UVB arms are satisfactory, with no need for further adjustments but this is not the case for the VIS–NIR joint, as can be seen for J0043 in Fig. 3. For several objects, the slope of the VIS arm was adjusted based on comparison to SDSS (see Paper I for more details). We therefore allow our fitting to re-scale the *global* continuum up to 10 per cent in each of the regions covered by each arm (1200–2200 Å, 2200–4000 Å, 4000–9000 Å) to take into account the arm calibration uncertainties.

3.2 Blended iron lines

For an adequate modelling of $H\beta$ and $Mg\ II$ line profiles, it is crucial to first subtract the iron line emission, originating from a large number of blended features of $Fe\ II$ and $Fe\ III$. Generally, this is done by choosing the best fit broadened, shifted and scaled empirical iron line template. We constrain line centre shifts to be smaller than 1000 km s⁻¹ and broadening is constrained to the range 1000–20 000 km s⁻¹. For the optical region around $H\beta$ (4000–7000 Å), we used the iron template from Boroson & Green (1992). For the UV region around $Mg\ II$ (1700–3647 Å), we initially used the Tsuzuki et al. (2006, hereafter T06) template. However, the fits obtained using this template was not satisfactory, mainly due to an overestimation of the continuum emission. We therefore built a new iron template (see Appendix B and Fig. B1) based on the spectrum of I Zw 1 reported by T06, which is a composite of their UV (*HST*) observation and the optical (KPNO) observation reported by Laor et al. (1997).

One of the main differences between the *local* and *global* approaches is that under the *local* approach different scaling factors for the UV iron template at each side of the $Mg\ II$ line are required in order to guarantee an acceptable match to the observed spectrum. The scale factor in the red side of $Mg\ II$ is found to be always larger than the one for the blue side, but by no more than 10 per cent. This type of correction is not needed in the *global* approach, when the complete continuum model (AD+BC) is considered. Given that under the *local* approach the BC cannot be accounted for directly and that the BC is monotonically increasing from 2200 to 3647 Å, we suspect that the larger scale factor in the red side of $Mg\ II$ might be due to the BC and not to intrinsic changes in iron line emission.

3.3 Emission line measurements

For the emission line modelling, we have followed a procedure similar to the one described in TN12 (see their appendix C) and S07. In short, after removing the continuum emission (following either the *local* or *global* approaches) and the iron template, we

model the prominent broad emission lines with two broad Gaussian components. We allow for a range of line widths and shifts for each component, where the FWHM ranges between 1000 and 10 000 km s⁻¹ and the line shifts are limited to ± 1000 km s⁻¹ for the $H\alpha$, $H\beta$ and $Mg\ II$ lines, while for the $C\ IV$ line we allowed blueshifts of up to -3000 km s⁻¹. These different choices are motivated by the findings of several earlier studies (e.g. Vestergaard & Peterson 2006; S07; Park et al. 2013; R13). In the case of doublet lines ($C\ IV$ and $Mg\ II$), we used four Gaussians, forcing the two broad and two narrower components to have the same profiles and intensity, and the theoretical wavelength separation. We fixed the $Mg\ II$ and $C\ IV$ doublet intensity ratios to 1:1, suitable for optically thick line emission. For each of the $H\alpha$, $H\beta$ and $C\ IV$ lines, we have also included a third Gaussian component when needed to account for the additional emission originating from the narrow line region (NLR). Each of these narrow components are modelled by a single Gaussian profile, their FWHM is constrained not to exceed 1300 km s⁻¹ and their line centres are tied to each other, with shifts of 400 km s⁻¹, at most. We chose not to include a narrow component in the modelling of the $Mg\ II$ and $C\ IV$ lines (as in e.g. Wills et al. 1993; Sulentic et al. 2007), since we found no significant difference in the $Mg\ II$ measurements (or fit quality) when trying to include it.¹ For other, weaker emission lines (including $He\ II\ 1640$, $N\ IV\ 1718$, $Si\ III\ 1892$), we used only a single Gaussian component. These lines are not necessary for the purpose of this work except for limiting the continuum placement. More accurate modelling of these lines will be a topic of the fourth paper in this series.

All the Gaussian components we used are symmetric and defined by three parameters: peak flux density, FWHM and central wavelength. We have made several simple, physically motivated simplifying assumptions, in order to minimize the number of free parameters: the Gaussian components of lines of the same species were forced to share an identical width; we have also tied together the relative shifts in the central wavelengths of some lines, based on their laboratory wavelengths; and assume line-intensity ratios for some lines based on their statistical weights (see Appendix D and Table D1 for further details on the different emission line parameters, their assumed ranges, interconnections and delimitation of the emission line regions). Our line fitting procedure runs separately on each of the main emission line regions, while all the lines in each line region are fitted simultaneously.

Generally, the *global* (see Fig. 3) and *local* (see Fig. 4) continuum approaches follow the same line fitting procedures in terms of the number of components per emission line and the way they are tied together. One important difference is that in the *global* approach, the $C\ III]$ and $C\ IV$ line regions are considered a single region and are therefore fitted simultaneously. The reason for this is that under the *local* approach we take as continuum windows the region around 1700 Å following the same procedure of previous works (e.g. S07; TN12; and references therein). However, this region is usually contaminated by weak emission lines such as $N\ IV\ 1718$, and consequently, the thin disc continuum fit does not allow us to fit $C\ IV$ and $C\ III]$ independently.

In order to account for possible uncertainties in our spectral measurements, we performed 100 Monte Carlo realizations for each of the spectra. In each of these realizations, the flux density at each spectral pixel was altered from the observed value by a random, normally distributed value, assuming the corresponding level of

¹ For example, for $C\ IV$ we find that a narrow component typically contributes ~ 3 per cent, and at most 6 per cent, of the total line luminosity.

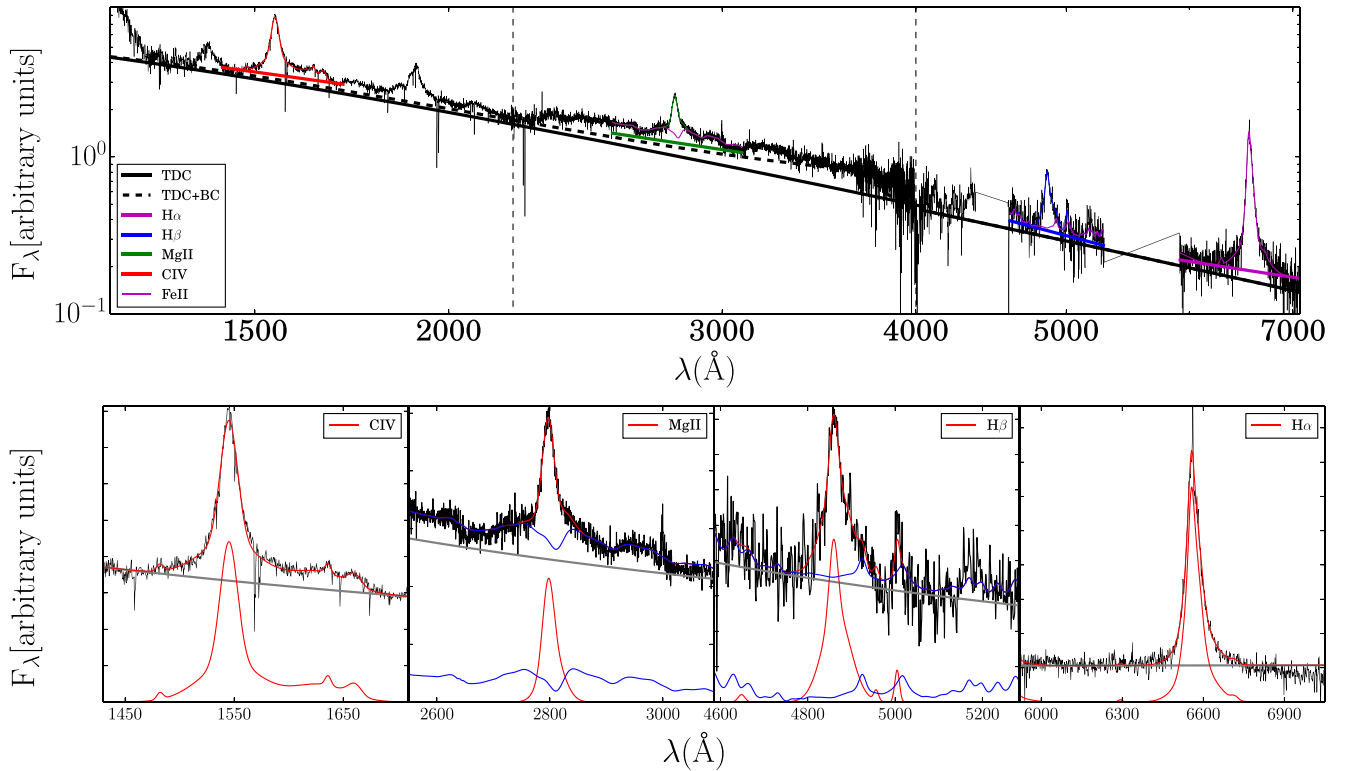


Figure 4. An example spectrum and spectral decomposition of one of the sources in our sample, J0143–0056 using the *local* approach. The top panel presents the rest-frame X-Shooter spectrum and the overall decomposition. The solid black solid line corresponds to the ‘thin disc’ continuum, while the dashed black line illustrates the addition of the BC. We highlight the spectral regions surrounding the most prominent broad emission lines (from left to right: C IV in red, Mg II in green, H β in blue and H α in magenta). The bottom panels show in detail the highlighted regions of the top panel as well as the individual *local* continuum determinations. Continuum fitting is in grey. Continuum plus iron emission fitting is in blue. Continuum plus, iron plus line fitting in red. Observed spectrum is in black.

noise (i.e. using the noise spectrum). From these sets of best-fitting models we extracted, for each emission line, the line width FWHM, the velocity dispersion (σ_{line} ; following Peterson et al. 2004), integrated luminosity (L), rest-frame equivalent width (EW), the luminosity at the peak of the fitted profile (L_p) as well as its corresponding wavelength (λ_p) and the offset of the line centre (relative to the laboratory wavelength; Δv). The line offsets were calculated using the flux-weighted central wavelength of the broad line profile:

$$\Delta v = \left(\int \lambda f_{\lambda}(\text{line}) d\lambda / F(\text{line}) - \lambda_0 \right) c / \lambda_0, \quad (2)$$

where $f_{\lambda}(\text{line})$ is the flux density of the broad line profile at λ ; $F(\text{line})$ is the integrated broad line flux, $F(\text{line}) = \int f_{\lambda}(\text{line}) d\lambda$; λ_0 is the laboratory wavelength of the line and c is the speed of light.

The best-fitting values for all these parameters were taken from the medians of the parameter distribution, and the corresponding uncertainties were estimated from the central 68 per cent percentiles. This ‘re-sampling’ approach for the estimation of measurement-related uncertainties was used in several recent studies of spectral decomposition of AGN UV–optical spectra (e.g. Shen & Liu 2012). Based on our experience, such errors reflect the true uncertainties related to measuring emission line profiles, while those provided by the (statistical) spectral fitting procedure itself tend to underestimate the ‘real’ uncertainties.

The measured parameters and uncertainties for the most prominent emission lines under the *local* approach are summarized in Tables 2 and 3. The data are also available at

http://www.das.uchile.cl/~jemejia/big_table_mass_paper.tar.gz which contains the plain text tables with these quantities in the *local* and *global* approaches as well as the FWHMs and σ_{line} s that we measured using the archival SDSS spectroscopy that covers both the C IV and Mg II lines.

4 RESULTS AND DISCUSSION

4.1 Local versus global continuum measurements

In this subsection, we compare the *local* and *global* continuum approaches in order to quantify the possible biases that are introduced when the real underlying shape of the continuum cannot be accurately established. As we will describe below in detail, our main conclusion is that *local* continuum measurements of FWHMs, continuum luminosities and, consequently, black hole masses present very small but systematic offsets with respect to the corresponding *global* continuum measurements.

4.1.1 Continuum biases

In Fig. 5, we present the comparison between L_{local} and L_{global} (top-left panel) for different chosen wavelengths. We generally find small but systematic offsets between quantities derived via the *local* versus *global* approach. We find that the L_{1450} , L_{3000} , L_{5100} and L_{6200} median offsets ($\Delta L \equiv \log(L_{\text{global}}/L_{\text{local}})$) are typically small ($\lesssim | -0.05 |$ dex, see Table 4 for details). These offset are consistent with

Table 3. Broad line widths and corresponding mass estimates, under the *local* approach.

Object name	FWHM(km s ⁻¹)				σ _{line} (km s ⁻¹)				-log(M _{BH} (FWHM)/M _⊙)				H α _{line} ^b													
	C IV	Δ	H α	Δ	C IV	Δ	H α	Δ	C IV	Δ	Mg II	Δ	H β	Δ	H α _{cont} ^a	Δ	H α _{line} ^b	Δ								
J1152+0702	6573.17	133.06	3202.24	135.98	4729.64	270.58	4283.31	240.51	3870.09	351.63	2165.29	179.2	4611.16	79.61	3186.29	246.89	9.65	0.02	9.44	0.06	9.48	0.05	9.32	0.06		
J10155-1023	6581.92	92.02	3468.25	66.93	5458.28	139.76	4785.95	115.95	5553.35	131.83	2113.16	129.33	2601.71	50.29	4010.01	147.36	9.54	0.01	9.46	0.02	9.58	0.03	9.51	0.02	9.46	0.03
J10303+0027	5913.74	185.57	4790.24	136.5	7342.45	165.96	6229.92	99.96	3856.09	381.76	2519.43	219.8	3883.75	61.91	4897.97	308.97	9.39	0.03	9.7	0.03	9.77	0.02	9.69	0.02	9.64	0.02
J1158-0322	4836.3	72.18	3375.87	132.76	5192.01	408.19	4854.6	169.2	2678.57	52.06	1900.87	106.72	4516.99	348.21	4114.39	261.77	9.21	0.01	9.39	0.04	9.5	0.08	9.47	0.03	9.44	0.04
J0043+0114	7323.78	120.88	3379.59	93.25	4057.87	492.7	3227.27	123.33	3628.23	30.2	2508.89	204.13	5328.8	93.02	6133.45	83.24	9.54	0.02	9.34	0.03	9.19	0.12	9.06	0.04	9.01	0.04
J0209-0947	5032.08	56.01	2900.08	64.16	5124.13	278.41	4722.6	176.26	4030.67	60.19	2298.9	145.81	4313.91	330.76	3973.72	146.8	9.26	0.01	9.28	0.02	9.5	0.06	9.46	0.04	9.44	0.04
J10842+0151	6524.91	109.83	3951.92	128.07	5231.26	563.34	4955.88	55.58	3625.84	233.43	2044.7	165.81	4408.65	196.49	5900.66	136.71	9.39	0.02	9.45	0.03	9.32	0.12	9.36	0.02	9.42	0.02
J1002+0331	5017.31	439.6	2563.88	69.75	5464.7	596.11	4738.24	81.6	2445.63	42.2	1854.53	235.07	4000.48	125.61	3315.12	276.48	9.12	0.03	9.49	0.11	9.44	0.02	9.44	0.02	9.43	0.02
J0323-0029	5189.8	68.08	1889.87	69.24	2990.6	446.07	3127.0	608.27	3283.82	57.48	3206.57	47.72	3441.97	173.99	2955.2	188.82	9.26	0.01	8.84	0.04	8.94	0.14	9.05	0.22	9.05	0.21
J0152-0839	6481.41	69.84	3116.09	158.2	4306.36	340.16	4813.74	164.25	3754.43	348.65	2110.44	186.45	3871.83	228.1	5716.66	259.13	9.34	0.01	9.18	0.05	9.18	0.08	9.28	0.03	9.29	0.04
J0941+0443	7721.23	63.08	4218.07	286.42	6151.72	308.41	6520.48	120.97	3811.46	34.47	2948.63	94.8	3823.26	430.01	4161.47	141.57	9.46	0.01	9.42	0.07	9.46	0.06	9.58	0.02	9.62	0.02
J0148+0003	6662.44	1461.18	4542.74	183.5	6474.99	340.44	5411.48	67.74	3844.55	258.27	2278.39	233.47	3458.09	114.54	4510.4	185.17	9.42	0.22	9.67	0.04	9.72	0.06	9.62	0.01	9.62	0.01
J0934+0005	6536.46	282.31	2806.89	57.93	2880.02	144.81	2694.27	163.45	2702.42	0.0	1635.09	235.95	2573.13	254.74	2995.19	596.9	9.25	0.04	8.98	0.02	8.73	0.05	8.73	0.06	8.71	0.06
J0019-1053	5219.79	89.76	4425.79	76.59	5708.5	376.28	5908.82	506.23	3484.23	195.22	2818.44	115.48	2849.73	479.65	4694.24	467.45	8.9	0.02	9.28	0.02	9.15	0.07	9.27	0.09	9.3	0.08
J0850+0022	6115.68	272.63	2415.05	123.67	3503.46	960.02	3763.47	149.19	2905.3	123.92	1749.98	437.53	4858.84	322.37	3435.86	135.78	8.98	0.04	8.73	0.05	8.8	0.29	8.93	0.11	8.84	0.11
J0404-0446	4341.32	304.12	1965.55	50.96	2788.42	1363.96	2731.63	140.01	1841.37	99.93	1666.83	264.0	867.64	230.43	6567.38	769.42	8.74	0.06	8.54	0.03	8.66	0.6	8.64	0.06	8.43	0.08
J1052+0236	9627.85	852.07	5412.1	422.04	10110.01	1132.0	8117.99	338.71	5192.56	272.53	2701.9	339.79	5726.97	567.53	4513.15	408.93	9.37	0.08	9.41	0.08	9.66	0.11	9.54	0.05	9.55	0.05
J0223-0007	5239.8	174.63	3077.91	80.99	3416.23	549.13	5009.03	271.49	3500.23	374.37	2425.53	288.24	5199.39	403.63	5461.09	1392.14	8.88	0.03	8.9	0.03	8.65	0.19	9.05	0.08	9.12	0.07
J0240-0758	5858.64	135.99	2827.82	94.14	3542.36	445.25	4189.8	158.88	3013.8	32.58	2184.61	133.16	5569.2	275.57	4136.64	445.19	9.0	0.02	8.88	0.03	8.75	0.13	8.95	0.04	9.03	0.04
J0136-0015	7051.94	114.59	3553.55	86.89	2730.93	1000.53	3467.62	276.33	4489.88	434.54	2248.54	192.31	3648.03	195.22	5068.74	586.32	9.1	0.02	9.01	0.03	8.43	0.42	8.68	0.08	8.76	0.08
J0213-1003	5093.2	167.27	2741.59	251.38	3392.86	279.21	4054.31	192.65	3523.3	932.25	1939.26	287.79	4174.0	871.34	4579.36	117.79	9.06	0.03	8.96	0.09	8.85	0.08	9.06	0.05	9.05	0.05
J0341-0037	5246.89	130.51	2571.38	106.3	3218.83	2612.53	3405.73	610.87	3982.5	398.66	1901.38	277.54	3567.48	736.67	4447.75	907.79	8.8	0.02	8.68	0.04	8.58	1.47	8.68	0.19	8.74	0.19
J0143-0056	3890.11	76.91	2856.85	107.36	5509.54	1371.7	3894.47	570.51	3277.0	107.64	1400.35	212.49	1876.82	121.42	4417.88	1204.3	8.54	0.02	8.75	0.04	8.97	0.26	8.72	0.16	8.78	0.16
J0927+0004	8307.68	152.96	5663.93	202.87	7418.97	915.99	6255.58	148.7	4555.5	291.75	2477.82	189.86	4265.65	355.71	4997.04	557.7	9.21	0.02	9.34	0.04	9.23	0.13	9.18	0.03	9.23	0.03
J0213-0036	4063.84	101.99	3462.69	155.4	5697.36	1018.59	4458.74	171.6	2719.59	41.51	1811.81	159.25	2680.4	569.02	4997.53	672.0	8.53	0.02	8.88	0.05	8.98	0.19	8.85	0.04	8.97	0.04
J1050+0207	7608.29	816.82	4888.94	762.65	5204.91	1493.81	5402.67	504.92	4416.38	210.67	2409.78	196.71	2442.51	345.5	5260.54	706.67	9.06	0.1	9.15	0.16	8.88	0.33	8.9	0.1	9.01	0.1
J0948+0137	5115.62	251.64	3363.61	331.15	3766.11	728.57	3880.89	392.36	3292.57	178.85	1997.33	367.65	3373.17	769.02	2879.06	1025.66	8.6	0.05	8.75	0.1	8.54	0.21	8.67	0.13	8.77	0.11
J0042+0008	5362.14	347.78	2943.94	120.79	4020.34	345.5	3607.54	160.39	4970.52	292.54	1843.64	224.51	4028.2	473.32	5323.33	540.12	8.64	0.06	8.58	0.04	8.5	0.11	8.44	0.06	8.54	0.06
J1013+0245	8990.08	304.21	4603.49	709.46	8395.63	1030.61	7716.39	872.62	1124.06	469.07	2678.99	213.54	6546.57	3016.95	3037.51	291.49	9.07	0.04	8.95	0.16	9.27	0.14	9.25	0.12	9.15	0.14
J1021-0027	4912.88	628.93	3260.01	159.14	9085.38	1675.61	8817.56	719.31	2790.07	42.82	2409.75	157.98	5060.65	525.81	4593.35	183.54	8.29	0.13	8.52	0.05	9.15	0.21	9.29	0.09	9.43	0.08
J0038-0019	4332.98	333.19	2656.77	189.51	3557.91	284.34	3303.65	118.2	3397.61	353.28	2036.88	227.39	5494.81	663.5	2146.07	272.75	8.26	0.08	8.35	0.07	8.33	0.1	8.39	0.04	8.34	0.04
J0912-0040	4884.79	331.59	3859.93	251.59	5803.7	3022.45	4746.34	227.74	3198.91	193.24	2002.02	195.75	2164.52	213.84	2015.46	581.81	8.37	0.07	8.65	0.07	8.71	0.73	8.66	0.07	8.65	0.07
J1048-0019	4755.88	649.8	2901.43	155.43	2278.84	350.3	2966.74	1312.75	3167.81	288.13	2260.65	203.08	967.48	372.04	1261.05	249.41	8.34	0.14	8.37	0.06	7.81	0.2	7.99	0.136	8.11	0.71
J1045-0047	6027.95	520.11	2832.87	308.37	9706.63	3147.47	4724.3	403.71	3841.54	183.51	2202.59	227.6	6403.41	1425.91	2820.17	151.58	8.44	0.1	8.29	0.11	8.9	0.38	8.46	0.11	8.6	0.1
J0042+0011	4917.93	217.44	1829.42	210.0	1578.09	122.63	1489.82	95.27	2929.25	161.1	1097.93	599.1	1701.43	475.43	1177.48	165.01	8.1	0.06	7.9	0.11	7.52	0.12	7.49	0.09	7.42	0.08
J1046+0025	3971.13	481.38	3210.69	164.83	4319.81	1113.03	3382.7	584.84	2207.23	226.84	1013.97	984.74	1003.89	1965.21	81.1	0.12	8.35	0.06	8.26	0.33	8.16	0.24	7.81	0.24	7.81	0.24
J0930-0018	6704.04	856.67	5058.85	416.66	7035.13	796.99	6079.72	7366.64	4590.25	423.08	3059.34	415.94	842.29	247.30	1508.94	1415.15	8.47	0.13	8.72	0.09	8.65	0.496	8.48	0.106	8.59	0.134
J1108+0141	7468.9	410.2	2601.39	91.7	4093.15	591.92	4750.88	63.75	3350.98	125.47	2830.93	118.89	3947.92	434.39	4184.72	134.75	9.59	0.05	9.24	0.04	9.37	0.14	9.52	0.01	9.42	0.02
J1005+0245	6095.34	1550.64	2475.74	144.98	3878.66	3284.9	5050.79	198.95	4574.16	128.83	1745.09	154.14	4291.27	196.04	4053.76	188.6	9.07	0.26	8.94	0.06	9.11	1.64	9.45	0.04	9.44	0.04

Notes. ^aM_{BH}(H α) measurements obtained through FWHM(H α) and L₀₂₀₀.

^bM_{BH}(H α) measurements obtained through FWHM(H α) and L(H α).

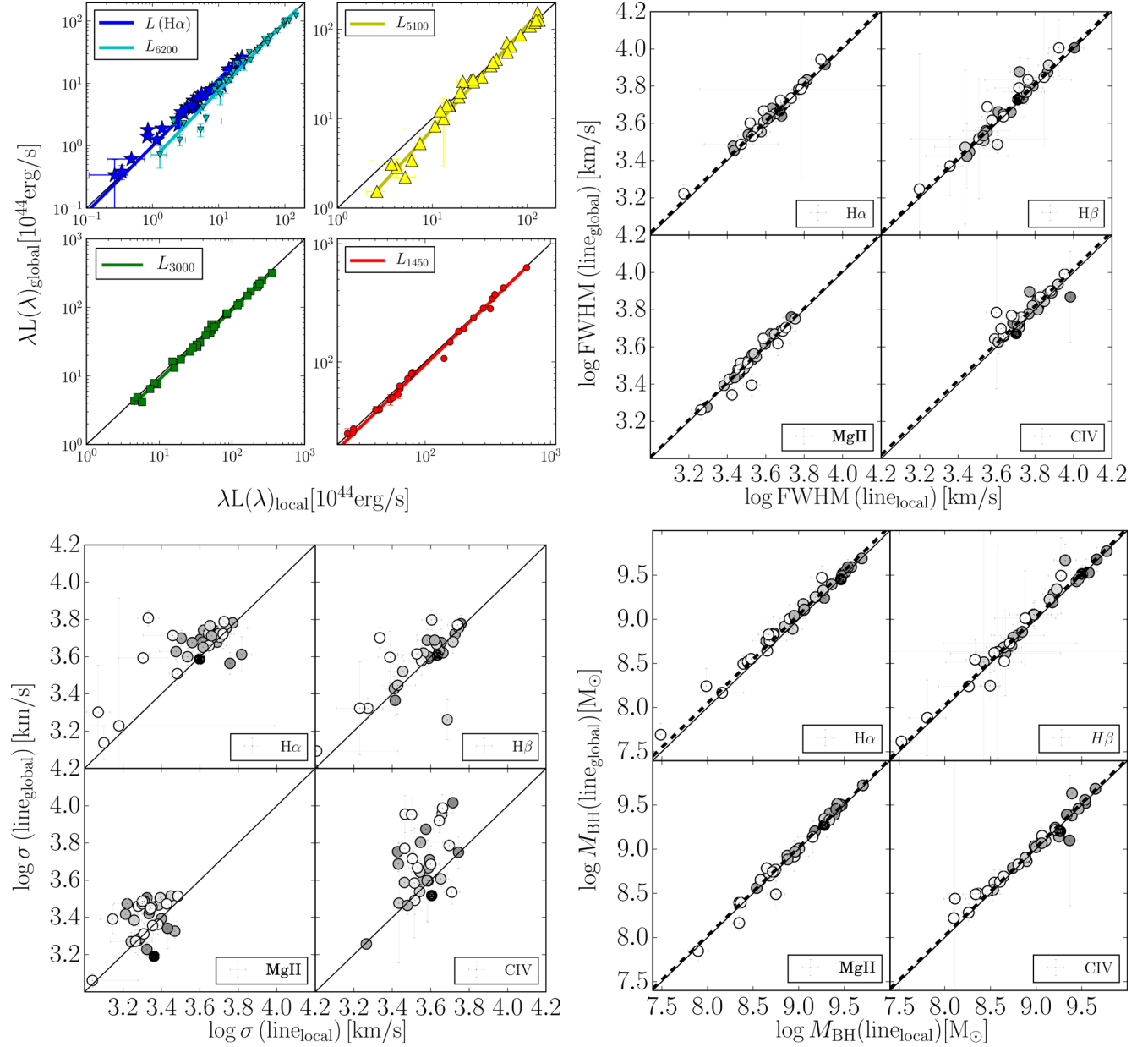


Figure 5. Comparison of various line and continuum properties measured under the two general assumptions of *local* (horizontal axis) and *global* (vertical axis) SEDs. Top-left panel: $L(\text{H}\alpha)$ (blue stars), L_{6200} (cyan triangles), L_{5100} (yellow triangles), L_{3000} (green squares) and L_{1450} (red dots). The coloured solid lines are the best linear fits to the corresponding data. Top-right panel: FWHM($\text{H}\alpha$) (top left), FWHM($\text{H}\beta$) (top right), FWHM(Mg II) (bottom left) and FWHM(C IV) (bottom right) lines measurements. Bottom-left panel: same as the top-right panel but comparing σ_{line} instead of FWHMs (note the much larger scatter in this case). Bottom-right panel: M_{BH} comparison between *local* and *global* approaches. In the top-right and bottom-right panels, black dashed lines represent the median offset between *global* and *local* measurements. In all panels, the black solid diagonal line represents the 1:1 relation. Points have been colour-coded in grey-scale by S/N where darker colours correspond to larger S/N.

Table 4. Median-induced offsets when the local approach is used instead of the *global* approach.

Line	ΔM_{BH} (dex)	ΔFWHM (dex)	ΔL (dex)	ΔL_{line} (dex)
$\text{H}\alpha$	$0.03^{+0.06}_{-0.06}$	$0.015^{+0.020}_{-0.015}$	$0.05^{+0.04}_{-0.06}$	$0.05^{+0.04}_{-0.06}$
$\text{H}\beta$	$0.04^{+0.09}_{-0.05}$	$0.020^{+0.035}_{-0.025}$	$-0.01^{+0.03}_{-0.05}$	$0.03^{+0.12}_{-0.05}$
Mg II	$0.01^{+0.03}_{-0.02}$	$0.010^{+0.015}_{-0.010}$	$-0.03^{+0.03}_{-0.02}$	$0.03^{+0.03}_{-0.03}$
C IV	$0.05^{+0.06}_{-0.03}$	$0.020^{+0.025}_{-0.020}$	$-0.02^{+0.02}_{-0.03}$	$0.07^{+0.06}_{-0.07}$

a very subtle overestimation of the continuum emission when the *local* approach is adopted (see Fig. 4 for a particular example).

4.1.2 Line width biases

The *systematic continuum overestimation* that we found coming from adopting the *local* instead of the *global* approach will naturally lead to *systematical FWHM underestimation* as can be also seen in Fig. 5 (top-right panel). Indeed, all the relevant line width measurements present small median offsets ($\Delta \text{FWHM} \equiv \log \text{FWHM}_{\text{global}} / \text{FWHM}_{\text{local}}$) smaller than $\lesssim 0.02$ dex as can be

seen in Table 4. As mentioned in Section 2, the measurements of $\text{FWHM}(\text{H}\beta)$ are more challenging for low S/N and/or objects where most iron emission is suppressed by telluric absorption. This explains the outliers and large uncertainties for some objects in the $\text{FWHM}(\text{H}\beta)_{\text{local}}-\text{FWHM}(\text{H}\beta)_{\text{global}}$ plot. Except for these few outliers, the $\text{FWHM}_{\text{local}}$ measurements of all the emission lines are proportional to, and systematically but slightly smaller than the $\text{FWHM}_{\text{global}}$ measurements.

When we perform the same analysis on the velocity dispersion σ_{line} (see the bottom-left panel in Fig. 5), we find a large scatter (~ 0.14 dex) and usually weak, if any, correlations ($P > 0.01$) between the *local* and *global* measurements in $\text{H}\alpha$, Mg II and C IV . On the other hand, the $\text{H}\beta$ line shows a much tighter correlation ($r_s < 0.78$, $P = 2 \times 10^{-9}$) but the scatter is still very large (~ 0.12 dex). These results indicate a strong and perhaps non-linear dependence between the measured σ_{line} and the level of its local continuum. As a result σ_{line} -based determinations of M_{BH} may be unreliable for data of limited spectral coverage. In particular, such estimates may suffer from higher systematic uncertainties compared to those based on FWHM.

4.1.3 Black hole mass biases

In Section 4.4, we will describe in detail the methods that we follow for M_{BH} calibration using the *local* and *global* approaches. The form of the virial mass estimator (see equation 1) indicates that biases in M_{BH} determinations are mainly driven by the (small) line width biases. This is not the case for the continuum luminosity since one can, in principle, re-calibrate the $R_{\text{BLR}}-L$ relations to use either one of the *local* or *global* measured continuum luminosities, thus completely eliminating the systematic biases.

After following the procedure described in Section 4.4 and the strict virial assumption ($M_{\text{BH}} \propto \text{FWHM}^2$), we found that the M_{BH} median offsets ($\Delta M_{\text{BH}} = \log M_{\text{BH, global}}/M_{\text{BH, local}}$) are in very good agreement with our predictions, as can be seen in the bottom-right panel of Fig. 5 and are smaller than $\lesssim 0.04$ dex (see Table 4). From the values listed in Table 4 and from a visual inspection of Fig. 5, one can conclude that $\text{H}\alpha$, Mg II and C IV are consistent (within the scatter) with ΔM_{BH} being independent of M_{BH} . $\text{H}\beta$ is again a bit more complicated, due to the difficulties we mentioned above. However, after removing the low-quality outliers we eventually find $\text{H}\beta$ to be consistent with ΔM_{BH} being independent of M_{BH} . Among all the lines considered here, we find Mg II to be the one showing the smallest biases when following the *local* approach. This is somewhat surprising, given the several important spectral features (BC, Fe II lines) that are influencing this spectral region.

4.1.4 Line luminosity biases

Line luminosities are more sensitive to continuum placement than the other quantities we examined. Indeed, we found line luminosity median offsets ($\Delta L_{\text{line}} = \log L(\text{line})_{\text{global}}/L(\text{line})_{\text{local}}$) of $0.06^{+0.08}_{-0.08}$ dex, $0.03^{+0.06}_{-0.04}$ dex, $0.02^{+0.09}_{-0.08}$ dex and $0.05^{+0.04}_{-0.06}$ dex for C IV , Mg II , $\text{H}\beta$ and $\text{H}\alpha$, respectively. Furthermore, we find that the large scatter that is generally found in $\Delta L_{\text{C IV}}$, $\Delta L_{\text{Mg II}}$, $\Delta L_{\text{H}\beta}$ and $\Delta L_{\text{H}\alpha}$ is due to the fact that these quantities are anticorrelated with continuum luminosity. In particular, the relations between these line luminosity biases and L_{5100} show r_s correlation coefficients of -0.38 , -0.44 , -0.65 for C IV , Mg II , $\text{H}\beta$ and $\text{H}\alpha$, respectively. This implies that using the local approach to estimate line luminosities generally leads to an underestimation of the latter, and its effect is larger for

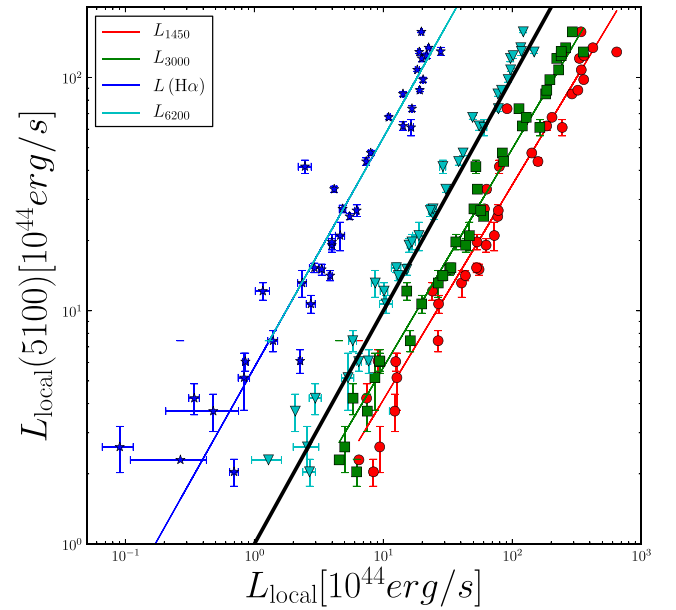


Figure 6. Local $\text{H}\alpha$ line luminosity (blue), L_{6200} (cyan), L_{3000} (green) and L_{1450} (red) versus L_{5100}^{local} . The colour solid lines represent the best linear fits to the corresponding data. The black solid line represents the 1:1 relation.

low-luminosity objects (up to 0.14 dex, or 38 per cent, in the case of C IV).

In summary, the impact of using the *local* approach to estimate the local luminosities, lines widths and black hole masses when the *global* continuum is unknown is found to be small (< 0.06 dex). However, the impact using the *local* approach to estimate line luminosities is found to be luminosity dependent, being stronger for low-luminosity objects. The median values of ΔFWHM , ΔL , ΔM_{BH} and ΔL_{line} that we found are summarized in Table 4. Based on the general good agreement between *local* and *global* measurements and in order to provide the community with strategies more applicable to observations with limited wavelength coverage, in the analysis that follows is based only on the local measurements, unless otherwise stated.

4.2 Luminosity correlations

Fig. 6 presents a comparison between L_{5100} and the luminosity indicators most commonly used in the context of M_{BH} estimates. The best-fitting parameters of all the correlations can be found in Table 5. These relations provide us with the links necessary to connect each luminosity indicator and $R_{\text{BLR}}(\text{H}\beta)$, through the $R_{\text{BLR}}-L_{5100}$ relation obtained from RM experiments (Kaspi et al. 2000, 2005; Bentz et al. 2009, 2013). For the purposes of this work, we use the same calibration as in TN12, which is appropriate for sources with $L_{5100} \gtrsim 10^{44} \text{ erg s}^{-1}$:

$$R_{\text{BLR}}(\text{H}\beta) = 538 \left(\frac{L_{5100}}{10^{46} \text{ erg s}^{-1}} \right)^{0.65} \text{ lt-days}. \quad (3)$$

As shown in Fig. 6 the $L(\text{H}\alpha)-L_{5100}$ relation shows a larger scatter than those involving UV continuum luminosities ($L_{1450}-L_{5100}$ and $L_{3000}-L_{5100}$). This may therefore contribute to an increased uncertainty in $L(\text{H}\alpha)$ -based determinations of M_{BH} . This is not surprising, given the expected range of conditions in the BLR. Consequently, we also investigate use of L_{6200} as an alternative to $L(\text{H}\alpha)$. As can be seen in Fig. 6 (cyan inverted triangles) the $L_{6200}-L_{5100}$ relation

Table 5. Best-fitting power-law parameters to the following relations: ${}^a L_{5100}^{\text{local}} = A L_{\text{local}}^\gamma$, ${}^b L_{5100}^{\text{local}} = A L_{\text{global}}^\gamma$, ${}^c L_{\text{global}} = A L_{\text{local}}^\gamma$.

	L_{5100}^{local} versus L_{local}^a		L_{5100}^{local} versus L_{global}^b		L_{global} versus L_{local}^c	
	γ	A	γ	A	γ	A
$L(\text{H}\alpha)$	1.04	4.73	1.09	3.59	0.94	1.32
L_{6200}	0.98	1.23	0.94	1.57	0.96	1.28
L_{5100}	1	1	0.89	1.61	1.15	0.60
L_{3000}	0.92	0.67	0.91	0.77	1.01	0.88
L_{1450}	0.88	0.56	0.87	0.64	1.02	0.87

shows an even smaller scatter than L_{1450} and L_{3000} . This is particularly the case for objects with $L_{5100} \gtrsim 10^{45} \text{ erg s}^{-1}$, where host galaxy contribution is negligible.

L_{1450} – L_{5100} and L_{3000} – L_{5100} luminosity correlations are supra-linear, in the sense of showing $L \propto L_{5100}^\beta$ and $\beta > 1$ (see the first column of Table 5 and note that $\beta = \gamma^{-1}$). This has been noted earlier by Vanden Berk et al. (2004) but is in contrast to Shen & Liu (2012) who found consistency with $\beta = 1$ in the sample of high-luminosity quasars ($L_{5100} [\text{erg s}^{-1}] > 10^{45.4}$).

While there are various correlations with $M_{\text{BH}}(\text{H}\alpha)$ and L/L_{Edd} (measured from $\text{H}\alpha$) that can, perhaps, explain these differences, it is important to note that our sample is by no means complete. It was chosen to sample the high- L $z=1.55$ AGN population by giving equal weight to a group of sources with the same M_{BH} and L/L_{Edd} (see Paper I). Hence, the relationship found here should be checked in a larger and complete sample that represents the entire AGN population.

4.3 Line widths and line offsets

4.3.1 Comparison with SDSS data

At the redshift range of our sample, the archival SDSS spectroscopy covers both the C IV and Mg II lines in 29 out of 39 objects.² In Fig. A1, we show an example of the SDSS and X-Shooter spectra in the overlapping region. Comparing SDSS and X-Shooter data allow us to test the effects of having only survey-grade data, with limited S/N and spectral resolution, on the measurement of line widths. To this end, we used our C IV and Mg II fitting code for the lower quality archival SDSS DR7 spectra. In Fig. 7, we compare the FWHM (top panels) and σ_{line} (bottom panels) values of the C IV and Mg II lines obtained from the SDSS data, with those obtained from our higher quality spectra under the *local* approach. We also show the Spearman correlation coefficients and corresponding P -values in each panel.

We find that SDSS-based FWHM(C IV) for objects with absorption features which are unresolved in the SDSS data (4 out of 29 objects, red symbols), or those with partially observed profiles because of the limited SDSS wavelength coverage (5 out of 29, yellow symbols) result in FWHM measurements which are systematically different from those obtained from the higher quality data. Specifically, while *unresolved absorption* features are likely to result in a systematic *underestimation* of FWHM(C IV), by about 50 ± 10 per cent, *incomplete* profiles are likely to lead to a systematic *overestimation* of FWHM(C IV), by about 40 ± 20 per cent. This result was found in previous works (e.g. D13; Park et al. 2013; Tilton & Shull 2013) and could explain, to some extent, the overpopulation

of narrow C IV objects that is reported in TN12. The Mg II line does not generally show strong absorption features. Indeed, we find that the SDSS-based FWHM(Mg II) measurements are generally consistent with our higher quality FWHM(Mg II) measurements with the exception of five objects. Of these five objects, three have very low S/N, one has an incomplete profile and one shows signs of absorption.

Looking into the corresponding comparison with σ_{line} (bottom panels of Fig. 7), we generally find that sources with absorption features or incomplete profiles do not stand out from the ‘normal’ population. The entire sample shows considerable scatter when comparing the SDSS and X-Shooter line measurements and show less significant correlations than the FWHM(top panels of Fig. 7). For $\sigma(\text{Mg II})$, we find the SDSS measurements to be systematically broader than our $\sigma_{\text{X-Shooter}}(\text{Mg II})$ estimations, and the scatter is larger than the one in the FWHM comparison. For $\sigma(\text{C IV})$, there is a large dispersion (0.2 dex) between SDSS and X-Shooter measurements that could be caused by the high sensitivity of σ_{line} measurements to continuum placement.

We conclude that the usage of σ_{line} to measure line width in data of limited quality introduces significant scatter. For such data, the use of FWHM is preferred, especially for the Mg II line. In addition, the absorption features often seen in the C IV line necessitate the use of high-quality spectra, in order to resolve and properly account for these features, even if one uses FWHM instead of σ_{line} .

4.3.2 Line offsets

We measured the line offsets with respect to the laboratory wavelengths of $\text{H}\alpha$, $\text{H}\beta$ and Mg II. Their absolute values ($|\Delta v|$) are found to be (within the 16 per cent and 84 per cent percentiles) smaller than 600, 550 and 250 km s^{-1} , respectively.

Many of the observed C IV lines show large negative velocity offsets ($\Delta v \simeq -1200 \pm 1000 \text{ km s}^{-1}$) suggesting non-virial equilibrium of the C IV-emitting clouds. This has been noted in numerous earlier publications (e.g. S07; Wang et al. 2009; Shen & Liu 2012; TN12; R13; Brotherton et al. 2015). Moreover, the C IV velocity offsets are anticorrelated with L/L_{Edd} ($r_s = -0.53$, $P = 0.0004$), i.e. higher L/L_{Edd} will translate into bluer line centres (e.g. Marziani, Dultzin-Hacyan & Sulentic 2006; Sulentic et al. 2007). We also find that the much smaller velocity offsets of the Mg II lines are also anticorrelated with L/L_{Edd} ($r_s = -0.49$, $P = 0.001$) which is also in agreement with M13. We repeated the analysis using the normalized accretion rate ($\dot{m} \equiv L_{\text{model}}/L_{\text{Edd}}[M_{\text{BH}}^{\text{model}}]$) taken from the best-fitting AD models (to be presented in Paper III; see Paper I for details). We find that our measured \dot{m} , too, is anticorrelated with C IV velocity offsets ($r_s = -0.49$, $P = 0.001$); however, the analogous correlation with Mg II velocity offsets becomes insignificant ($P = 0.07$). These results suggest that L/L_{Edd} is playing an important role in the line offsets of the C IV profile, while Mg II velocity offsets

² For the remaining 10 objects, the only archival spectroscopy available is from the 2SLAQ survey, which is of limited S/N and is not flux calibrated.

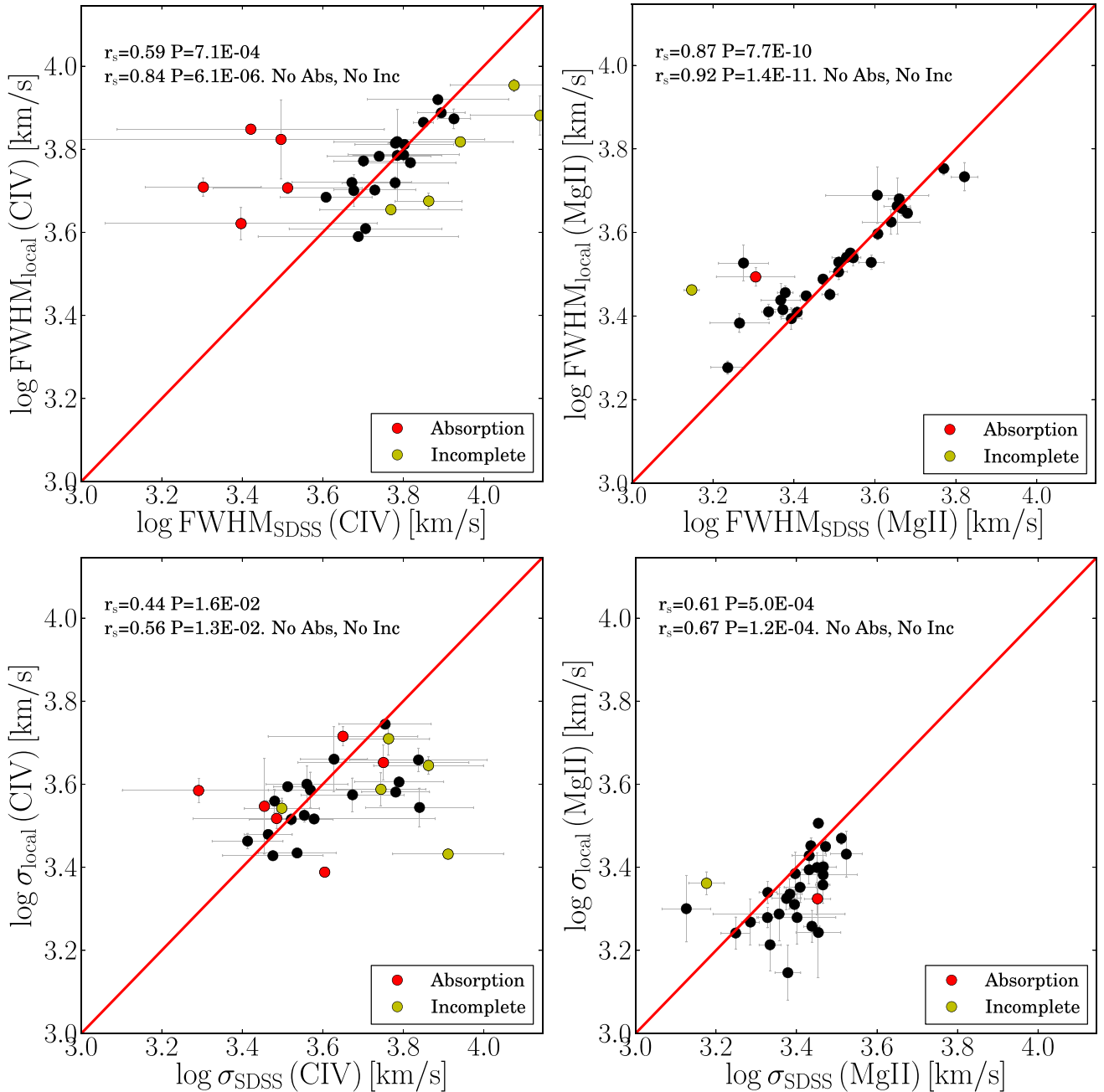


Figure 7. FWHMs (top panels) and σ_{line} s (bottom panels) of the C IV (left) and Mg II (centre) profiles found with low-quality SDSS data versus those measured in our high-quality X-Shooter using the *local* continuum approach. The right-hand panels show C IV versus Mg II line widths measured with SDSS data. The red solid line shows the 1:1 relation and the red dashed line represents $\text{FWHM}(\text{CIV}) = \sqrt{3.7} \text{FWHM}(\text{MgII})$. The red dots represent objects with noticeable absorption features while the yellow dots are objects with SDSS incomplete profiles. It can be seen that C IV profiles with strong absorption features artificially populate the zone where $\text{FWHM}(\text{CIV}) < \text{FWHM}(\text{MgII})$.

may involve additional parameters. As explained earlier, the way we selected our sample makes it difficult to make strong statements regarding the entire population of AGN. When the same analysis is done with the Balmer lines, we find no correlation between neither L/L_{Edd} nor \dot{m} and the Balmer line velocity offsets ($P = 0.26$ and $P = 0.90$, for $\text{H}\alpha$ and $\text{H}\beta$, respectively).

We further confirm earlier results (e.g. Corbin 1990; Richards et al. 2011) of a significant anticorrelation between the C IV blueshifts and the C IV line strength, $\text{EW}(\text{CIV})$ ($r_s = 0.43$, $P = 0.006$), but not with $\text{EW}(\text{MgII})$ ($r_s = 0.25$, $P = 0.12$).

Several studies investigated the possibility that broad emission lines are gravitationally redshifted by few hundred to few thousand km s^{-1} (e.g. Netzer 1977; Zheng & Sulentic 1990; Popovic et al. 1995; Müller & Wold 2006; Tremaine et al. 2014). This effect is enhanced in very broad emission line components ($\text{FWHM} \gtrsim 7000 \text{ km s}^{-1}$) that are formed close to the BH. In this work, we made no attempt to include this in the modelling of the line profiles since we are mainly after the line FWHM which is insensitive to such small variations. We verified, however, that line offset due to this effect are smaller than the general uncertainty and scatter associated

with our measurements of the line centre velocity. We come back to this issue in Paper IV (Mejía-Restrepo et al, in preparation).

4.3.3 Line width correlations

Fig. 8 presents a comparison between the widths of some of the broad emission lines in our X-Shooter observations, in terms of FWHM (top panel) and line dispersion (σ_{line} ; bottom panel). For reference, we also illustrate the 1:1 relation (black solid line), and a constant scaling of $\text{FWHM}(\text{C IV}) = \sqrt{3.7} \text{FWHM}(\text{H}\alpha, \text{H}\beta, \text{Mg II})$ (black dashed line). The latter scaling is motivated by the typical ratio of the corresponding BLR sizes for H β and C IV, as measured in RM experiments, and under the virialized BLR assumption (see detailed discussion in TN12). We have plotted in yellow a dashed line that represents $\text{FWHM}(\text{C IV}) = \sqrt{3.7} \left\langle \frac{\text{FWHM}(\text{H}\beta)}{\text{FWHM}(\text{H}\alpha, \text{Mg II})} \right\rangle \text{FWHM}(\text{H}\alpha, \text{Mg II})$ to account for the median FWHM ratio between FWHM(H β) and the FWHM of H α and Mg II. Finally, we have colour coded the points in grey-scale by the S/N of the continuum bands around H β where darker colours translates into higher S/N. In Figs C1 and C2 of Appendix C, we show the normalized H α , H β , Mg II and C IV observed line profiles in velocity space to provide the reader with a direct visual comparison of the most prominent emission lines. The large error bars in the H β line widths are due to the low S/N and the difficulty of constraining the iron emission around H β , because of the telluric absorption (see Section 2).

We generally find very good agreement between the FWHMs of H β and H α (Fig. 8, top-left panel). On average, $\text{FWHM}(\text{H}\beta)$ is broader than $\text{FWHM}(\text{H}\alpha)$ by 0.03 dex (see the blue dashed line in Fig. 8), with a scatter of about 0.08 dex. This result is in good agreement with several previous studies, as well as with the scaling relation reported in Greene & Ho (2005) (see the red dashed line in Fig. 8).

We also find that objects with $\log \text{FWHM}(\text{H}\beta) [\text{km s}^{-1}] \leq 3.6$ ($\sim 4000 \text{ km s}^{-1}$) show $\text{FWHM}(\text{H}\beta)$ slightly narrower than the median trend (i.e. below the blue dashed line in Fig. 8) by about 0.04 dex (10 per cent). These objects are however fainter and their values are less accurate because of the difficulties with H β measurements. This results is in agreement with Denney et al. (2009) where they found that the estimated $\text{FWHM}(\text{H}\beta)$ in low-quality data ($S/N \lesssim 20$) is not reliable.

From Fig. 8, we can also see that there are significant correlations between the FWHMs of (1) H α and Mg II (scatter of $\sigma_{\Delta} = 0.08$ dex), (2) H β and Mg II ($\sigma_{\Delta} = 0.10$ dex) and (3) H α and H β ($\sigma_{\Delta} = 0.07$ dex) in agreement with several previous works (e.g. Greene & Ho 2005; S07; Wang et al. 2009; Shen & Liu 2012; TN12; M13). Also, $\text{FWHM}(\text{Mg II})$ is proportional to and narrower than $\text{FWHM}(\text{H}\beta)$ by 0.16 dex (30 per cent), with a scatter of about 0.08 dex and no dependence on $\text{FWHM}(\text{H}\beta)$. There are however some outliers in these general trends: The two broad absorption line quasars (BALQSOs, the green dots in Fig. 8) and five objects that show $\text{FWHM}(\text{Mg II}) \gtrsim \text{FWHM}(\text{H}\beta)$ and have high $L/L_{\text{Edd}} (> 0.17$, hereafter broad-Mg II objects, magenta diamonds in Fig. 8). These seven objects and their implications in the $\text{FWHM}(\text{Mg II})$ -Balmer lines correlations are further discussed in Section 4.3.4.

From the discussion above, it is reasonable to assume that the emissivity-weighted Mg II region is more distant from the central BH than the corresponding regions for the H α and H β lines. On the other hand, both Balmer lines seem to come from the same part of the BLR. As a consequence and based on the FWHM linear

correlation among H α , H β and Mg II, assuming virialization of H β would reasonably imply virialization of Mg II and H α .

The correlations of $\text{FWHM}(\text{C IV})$ with the measured FWHM of the other lines are weaker, occasionally insignificant (i.e. $P > 0.01$) and non-linear: (1) H α ($r_s = 0.48$, $P=0.02$, $\sigma_{\Delta} = 0.14$ dex), (2) H β (insignificant, $P=0.05$) and (3) Mg II ($r_s = 0.50$, $P=0.001$, $\sigma_{\Delta} = 0.10$ dex). This would mean that $\text{FWHM}(\text{C IV})$ is not linearly proportional to the FWHM of H α , H β and Mg II. For example, $\text{FWHM}(\text{C IV}) \propto \text{FWHM}(\text{H}\alpha)^{1.41 \pm 0.50}$. Moreover, when combining the results of the RM experiments (e.g. Kaspi et al. 2007) with the virial assumption, it is expected that the C IV line would be broader than H β , by a factor of about $\sqrt{3.7}$.³ In contrast, the vast majority of sources in our sample (35/39; 90 per cent) show $\text{FWHM}(\text{C IV}) < \sqrt{3.7} \text{FWHM}(\text{H}\beta)$ and one-third of the sources have $\text{FWHM}(\text{H}\beta) > \text{FWHM}(\text{C IV})$. These results indicate either a non-virialized C IV emission region, or a very different ionization structure for objects with low and high $\text{FWHM}(\text{H}\beta)$.

Finally, when we compare the velocity dispersion (σ_{line}) between the lines of interest (bottom panels of Fig. 8), we only find one significant correlation between $\text{FWHM}(\text{Mg II})$ and $\text{FWHM}(\text{C IV})$ ($r_s = 0.43$, $P=0.005$) in the *local* approach. However, even this correlation does not hold under the *global* approach ($P = 0.36$). Due to the fact that the correlations between the FWHM of different lines are much tighter than the σ_{line} correlations (under both continuum approaches), and the fact that σ_{line} is strongly affected by flux in the line wings, we choose to use the FWHM to estimate M_{BH} in the analysis that follows.

4.3.4 Broad-Mg II and BALQSO objects

As discussed in Section 4.3, we found that Mg II profiles are generally and systematically narrower than H α and H β profiles. However, the top-right and top-centre panels of Fig. 8 show that around $\log(\text{FWHM}(\text{H}\beta))$ and $\log(\text{FWHM}(\text{H}\alpha) [\text{km s}^{-1}]) \lesssim 3.6$ ($\leq 4000 \text{ km s}^{-1}$) there are a handful of objects (magenta diamonds) that show $\text{FWHM}(\text{Mg II}) \gtrsim \text{FWHM}(\text{H}\alpha, \text{H}\beta)$ and were noted earlier as ‘broad-Mg II objects’.

Marziani et al. (2013b) and M13 presented a thorough eigenvector 1 analysis of the Mg II and H β profiles following Sulentic et al. (2002) from an SDSS-selected sample of 680 quasars. Their classification is based on the location of type I AGN in the $R_{\text{op}}\text{-FWHM}(\text{H}\beta)$ plane, where $R_{\text{op}} = L(\text{Fe II } 4750\text{\AA}) / L(\text{H}\beta)$. They claimed that the so-called Broad-Mg II objects belong to the extreme population A category (A3 and A4 according to their classification, see fig. 8 in M13) and represents about 10 per cent of the total population of high-luminosity AGN. These extreme population A objects have narrow H β profiles ($\leq 4000 \text{ km s}^{-1}$) and the highest R_{op} values. They are also among the objects with the highest Eddington ratios and largest velocity offsets. Unfortunately, our difficulties to properly measure the Fe II emission around H β do not allow us to measure R_{op} and test their assumptions. We can however compare their L/L_{Edd} estimates to our H α -based L/L_{Edd} estimates by applying a bolometric correction as described in TN12. As can be seen in Fig. 1, all these objects occupy the top 20 percentile of the L/L_{Edd} distribution in our sample ($L/L_{\text{Edd}} \geq 0.20$) in agreement with M13. The broad-Mg II objects in our sample also show relatively large C IV and Mg II velocity blueshifts (top 20 per cent, $\Delta v_{\text{Broad-Mg II}}(\text{C IV}) \lesssim -2200 \text{ km s}^{-1}$, $\Delta v_{\text{Broad-Mg II}}(\text{Mg II}) \lesssim -200 \text{ km s}^{-1}$) which is also in agreement

³ The scaling factor is somewhat luminosity dependent. See TN12 for a discussion of this issue.

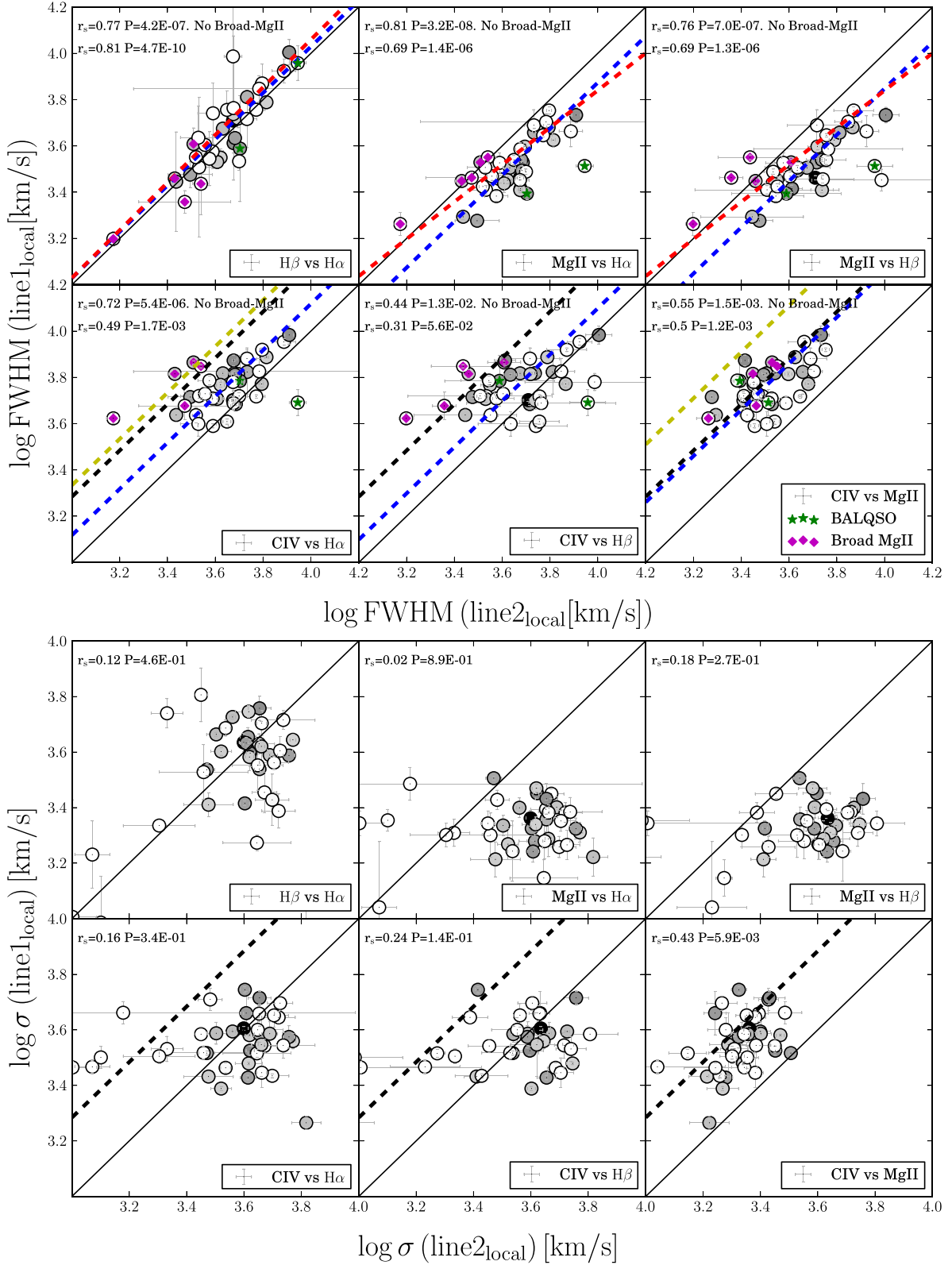


Figure 8. FWHM (top) and σ (bottom) comparisons between different lines in the local continuum approach as indicated in the inserts of each panel (line1 versus line2). The black solid lines represents the 1:1 relation. The black dashed line represents $\text{FWHM}(\text{CIV}) = \sqrt{3.7} \text{FWHM}(\text{line})$. The yellow dashed line represents $\text{FWHM}(\text{CIV}) = \sqrt{3.7} \text{FWHM}(\text{H}\beta)$ after re-scaling the FWHM of each line to $\text{FWHM}(\text{H}\beta)$ using the median value of $\text{FWHM}(\text{H}\beta)/\text{FWHM}(\text{line})$. The red dashed lines represent previous scaling relations [$\text{FWHM}(\text{H}\beta)$ versus $\text{FWHM}(\text{MgII})$ from TN12, and $\text{FWHM}(\text{H}\beta)$ versus $\text{FWHM}(\text{H}\alpha)$ from Greene & Ho (2005)]. The blue dashed lines represent the best fit after assuming $\text{FWHM}(\text{H}\beta) \propto \text{FWHM}(\text{H}\alpha) \propto \text{FWHM}(\text{MgII}) \propto \text{FWHM}(\text{CIV})$. Points are colour-coded in grey-scale by the S/N of the continuum bands around $\text{H}\beta$ where darker colours translates into larger S/N. Broad absorption lines quasars (BALQSO, green stars) and the broad-Mg II objects (magenta diamonds, see Section 4.3.4) are the main sources of discrepancies of the CIV and MgII FWHMs when compared to the $\text{H}\alpha$ and $\text{H}\beta$ FWHMs.

Table 6. Line width ratios and correlations. For each pair of lines, we list median values and scatter of $Q \equiv \log(\text{FWHM}(\text{line1})/\text{FWHM}(\text{line2}))$ and the Spearman correlation coefficients between $\text{FWHM}(\text{line1})$ and $\text{FWHM}(\text{line2})$. We tabulate these quantities for both the complete sample (under the *local* approach), and after excluding the five broad-Mg II and the two BALQSO.

line1	H α						Mg II						C IV					
	—All objects ^a —			—No broad-Mg II ^b —			—All objects ^a —			—No broad-Mg II ^b —			—All objects ^a —			—No broad-Mg II ^b —		
	Q	scatter	r_s	Q	scatter	r_s	Q	scatter	r_s	Q	scatter	r_s	Q	scatter	r_s	Q	scatter	r_s
H α	–	–	–	–	–	–	0.13	0.08	0.69	0.13	0.07	0.81	–0.12	0.14	0.48	–0.11	0.10	0.72
Mg II	–0.13	0.08	0.69	–0.13	0.07	0.81	–	–	–	–	–	–	–0.26	0.10	0.50	–0.25	0.10	0.55
H β	0.03	0.07	0.81	0.04	0.07	0.77	0.15	0.10	0.69	0.16	0.08	0.88	–0.10	0.17	0.31	–0.09	0.13	0.44

Notes. ^aIncluding all objects in the local approach.

^bWithout considering the Broad MgII and BALQSO objects.

with M13. We note however that broad-Mg II objects are not the only ones that meet the mentioned conditions.

As can be seen in Fig. 8, the BALQSOs in our sample show exactly the opposite behaviour. They show narrower Mg II profiles than usual. Unfortunately, it is impossible to draw any conclusion based on only two sources.

In Table 6, we present the median values and corresponding scatter of $Q \equiv \log(\text{FWHM}(\text{line1})/\text{FWHM}(\text{line2}))$ as well as the Spearman correlation coefficient between the FWHM of the listed lines under two cases: (a) including *all* objects in the analysis and (b) excluding the broad-Mg II and the BALQSOs from the analysis. It can be seen in Table 6 and Fig. 8 that after removing these outliers the FWHM correlations becomes tighter (i.e. r_s increases) and the Q factors remain almost unchanged. We emphasize that this result is also true for $\text{FWHM}(\text{C IV})$ while the correlations between $\text{FWHM}(\text{C IV})$ and the FWHM of the Balmer lines approach to linearity after removing such seven objects. Consequently, for the following M_{BH} analysis we exclude both the five broad-Mg II objects and the two BALQSOs.

4.4 Black hole mass estimators

In this subsection, we present the procedure we use to obtain, and compare, different M_{BH} estimates using the different line and continuum measurements. Our starting point, and the basis for all the following correlations, is the subsample of 32 AGN obtained by removing from the original sample five sources showing large discrepancy between $\text{FWHM}(\text{H}\beta)$ and $\text{FWHM}(\text{Mg II})$ (see Section 4.3.4) and the two BALQSOs in the sample. A major aim is to find a practical strategy that will allow the identification of sources that are not suitable for accurate mass determination based on single line and continuum measurement.

4.4.1 L_{5100} – $R_{\text{BLR}}(\text{H}\beta)$ relation and $\text{H}\beta$

Most present-day single-epoch mass measurements are based on the $R_{\text{BLR}}(\text{H}\beta)$ – L_{5100}^{local} relation, established through RM experiments (see Section 1 and equation 3). In this case, L_{5100}^{local} is a *local* estimation of the continuum and R_{BLR} is obtained from the time lag of the response of the $\text{H}\beta$ line to (optical) continuum variations. This lag is assumed to properly represent the emissivity weighted radius of the broad $\text{H}\beta$ line. M_{BH} is obtained from equation (1) where both $\text{FWHM}(\text{H}\beta)_{\text{local}}$ and L_{5100}^{local} are obtained using *local* continuum measurements. These values can be used to obtain the ‘local’ BH mass estimate, M_{BHlocal} . We can then use the expressions derived in Section 4.2, and the various biases between the *local* and *global* L_{5100} and FWHM, to derive a *global* expression for $M_{\text{BH}}(\text{H}\beta)$.

We start by using the local $M_{\text{BH}}(\text{H}\beta)$ expression obtained by TN12. This expression is most appropriate for our intermediate- and high-luminosity AGN:

$$M_{\text{BH}}(\text{H}\beta)_{\text{local}} = 5.26 \times 10^6 M_{\odot} \left(\frac{L_{5100}^{\text{local}}}{10^{44} \text{ erg s}^{-1}} \right)^{0.65} \times \left(\frac{\text{FWHM}(\text{H}\beta)_{\text{local}}}{10^3 \text{ km s}^{-1}} \right)^2. \quad (4)$$

Obtaining the equivalent *global* expression is not trivial since we need first to find a relation between R_{BLR} measured from RM and L_{5100}^{global} and not simply use the recipe that connects local measurements. However, we do not know L_{5100}^{global} for the objects targeted by RM campaigns, and we have to rely on the scaling relation between L_{5100}^{local} and L_{5100}^{global} that we find in this work (see Table 5). Substituting in equation (3), we get

$$M_{\text{BH}}(\text{H}\beta)_{\text{global}} = 7.17 \times 10^6 M_{\odot} \left(\frac{L_{5100}^{\text{global}}}{10^{44} \text{ erg s}^{-1}} \right)^{0.58} \times \left(\frac{\text{FWHM}(\text{H}\beta)_{\text{global}}}{10^3 \text{ km s}^{-1}} \right)^2. \quad (5)$$

It is important to note that we have simply re-scaled the empirical $R_{\text{BLR}}(\text{H}\beta)$ versus L_{5100}^{local} relation to a $R_{\text{BLR}}(\text{H}\beta)$ versus L_{5100}^{global} relation that is adjusted to predict the *same* R_{BLR} measurements. Consequently, we do not expect any systematic bias in M_{BH} measurements coming from intrinsic $L_{5100}^{\text{global}} - L_{5100}^{\text{local}}$ biases. The bias between M_{BHlocal} and M_{BHglobal} are simply the results of the intrinsic differences between the $\text{FWHM}_{\text{local}}$ and $\text{FWHM}_{\text{global}}$ (see Section 4.1). The small M_{BH} biases that we found are shown in the bottom-right set of panels in Fig. 5.

4.4.2 Other lines

In order to calibrate H α , Mg II and C IV line measurements to match the $M_{\text{BH}}(\text{H}\beta)$ predictions, we follow standard procedures (e.g. McLure & Dunlop 2004; Vestergaard & Peterson 2006; TN12) that basically re-scale $R_{\text{BLR}}(L_{5100})$ to $R_{\text{BLR}}(L_{\lambda})$ (see equation 3) and then re-scale $\mu(\lambda)$ to $M_{\text{BH}}(\text{H}\beta)$, where $\mu(\lambda) = G^{-1} R_{\text{BLR}}(L_{\lambda}) \text{FWHM}(\text{line})^2$.

This approach assumes that M_{BH} scales as FWHM^2 , which follows from a virialization of the line-emitting region. According to the direct proportionality that we found between $\text{FWHM}(\text{H}\beta)$, $\text{FWHM}(\text{H}\alpha)$ and $\text{FWHM}(\text{Mg II})$ (see Section 4.3), it will be enough to assume virialization of the $\text{H}\beta$ -emitting region. We note that several previous studies have instead allowed total freedom to the dependence of M_{BH} on FWHM (e.g. Shen & Liu 2012), instead of assuming a virial relation. However, there is no physical motivation for this approach (except perhaps for C IV) apart from the

Table 7. Virial BH mass calibrations of equation (1) ($M_{\text{BH}} = K(L_{\lambda})^{\alpha} \text{FWHM}^2$) based on different line width and luminosity combinations for 32/39 objects in our sample, calibrated against the $\text{H}\beta$ virial mass calibration given in equation (4). ^a M_{BH} calibration based on *local* measurements. ^b M_{BH} calibration based on *global* measurements. ^cLocal M_{BH} calibrations corrected for the *small* systematic offsets that we found with respect to *global* M_{BH} . Note that the values in this table are valid for L in units of $10^{44} \text{ erg s}^{-1}$ and FWHM in units of 1000 km s^{-1} . For these calibration, we assume $f = 1$ which is appropriate for FWHM M_{BH} estimates.

	Local ^a			Global ^b			Local ^b _{corr}		
	log K	α	Scatter (dex)	log K	α	Scatter (dex)	log K	α	Scatter (dex)
FWHM($\text{H}\alpha$), L_{5100}	6.779	0.650	0.16	6.958	0.569	0.19	6.845	0.650	0.16
FWHM($\text{H}\alpha$), L_{6200}	6.842	0.634	0.16	7.062	0.524	0.22	6.891	0.634	0.16
FWHM($\text{H}\alpha$), $L(\text{H}\alpha)$	7.072	0.563	0.18	7.373	0.514	0.23	7.389	0.563	0.18
FWHM($\text{H}\beta$), L_{5100}	6.721	0.650	0.00	6.864	0.568	0.00	6.740	0.650	0.00
FWHM(Mg II), L_{3000}	6.906	0.609	0.25	6.955	0.599	0.29	6.925	0.609	0.25
FWHM(C IV), L_{1450}	6.331	0.599	0.33	6.349	0.588	0.38	6.353	0.599	0.33

attempt to minimize residuals with regard to $M_{\text{BH}}(\text{H}\beta)$. We focus on identifying those sources which appear to represent the largest deviation from virial equilibrium, and excluding them from the analysis. As explained in Section 4.3.4, these are the five sources with the largest deviations between FWHM($\text{H}\beta$) and FWHM(Mg II) that are mostly small width (FWHM($\text{H}\beta$) $< 4000 \text{ km s}^{-1}$), high L/L_{Edd} ($\gtrsim 0.17$) sources and the two BALQSOs. In such cases, $M_{\text{BH}}(\text{H}\alpha)$ and $M_{\text{BH}}(\text{H}\beta)$ are the only methods providing reliable M_{BH} determination.

The results of the re-scaled single-epoch M_{BH} estimators based on $\text{H}\alpha$, $\text{H}\beta$, Mg II and C IV in 32/39 sources are summarized in Table 7 and shown in Fig. 9 where the black solid lines represent the 1:1 relations. We also show the seven removed sources: BALQSOs in green and objects with discrepant FWHM($\text{H}\beta$) and FWHM(Mg II) in magenta.

Fig. 9 shows that the main sources of scatter in all the M_{BH} relationships in the original sample are the above-mentioned seven sources. Removing these objects leaves almost perfect correlations ($r_s > 0.85$, $P < 10^{-12}$) between mass estimates based on $\text{H}\alpha$, $\text{H}\beta$ and Mg II and even C IV . In fact, the scatter in $M_{\text{BH}}(\text{H}\alpha) - M_{\text{BH}}(\text{Mg II})$ and $M_{\text{BH}}(\text{H}\alpha) - M_{\text{BH}}(\text{C IV})$ is reduced from 0.23 to 0.15 dex and from 0.29 to 0.16, respectively, for the L_{6200} -FWHM($\text{H}\alpha$) estimates. Unfortunately, it is not easy to identify and remove such objects from a sample where only the C IV line region is observable. We come back to this issue later in the paper.

The use of $L(\text{H}\alpha)$ in Xiao et al. (2011), as well as other studies (e.g. Greene & Ho 2005), is motivated by the possibility of host-light contribution to L_{6200} , especially in low-luminosity (low-redshift) AGN. However, as previously mentioned (Section 3), most of our objects have negligible host galaxy contamination, and we have accounted for it in the few objects where it is relevant. Thus, we can safely use L_{6200} for $\text{H}\alpha$ -based M_{BH} estimates. In Table 7, we present both L_{6200} -FWHM($\text{H}\alpha$) and $L(\text{H}\alpha)$ -FWHM($\text{H}\alpha$) M_{BH} calibrations.

In Fig. 9, we also present the best-fitting relations that compare our new mass prescriptions with previously published ones (black dashed lines). Particularly, we compared our new calibrations with the TN12 Mg II -based calibration, the Xiao et al. (2011) $\text{H}\alpha$ -based calibration (an updated version of Greene & Ho 2005) and the Vestergaard & Peterson (2006) C IV -based calibration. We note that these are somewhat simplified comparisons, as a proper analysis of the deviation from each M_{BH} calibration is not straightforward, due to the usage of different f factors; different $R_{\text{BLR}}-L$ relations; assumed cosmology; and even of fitting procedures. Nevertheless, it is evident from the diagram that the deviation from the earlier mass

estimates based on C IV are the largest among the three (bottom panel of Fig. 9).

4.4.3 X-Shooter versus SDSS M_{BH} estimates

In Fig. 10, we compare the M_{BH} estimations using the (lower S/N) SDSS spectra and (higher S/N) X-Shooter spectra, by plotting $\Delta \log M_{\text{BH}} \equiv \log(M_{\text{BH}}(\text{line})/M_{\text{BH}}(\text{H}\alpha))$ for Mg II and C IV versus the S/N of the continuum around $\text{Mg II}([S/N]_{\text{Mg II}})$. We note that the typical difference between the data sets is $(S/N)_{\text{XSh}} \simeq 4 \times (S/N)_{\text{SDSS}}$. As expected (see Section 4.3), objects with unresolved absorption features or incomplete line profiles generally show the largest offsets in mass. Apart from these objects, the scatter in $M_{\text{BH}}(\text{C IV})$ and $M_{\text{BH}}(\text{Mg II})$ estimates is *independent* of the S/N. This is not surprising because of the good agreement between X-Shooter- and SDSS-based FWHM(C IV) measurements (see Section 4.3.1). We conclude that the scatter in Mg II - and C IV -based mass estimates is dominated by intrinsic differences between FWHM(Mg II)-FWHM(C IV) and FWHM($\text{H}\alpha$) as well as between L_{5100} - L_{3000} and L_{6200} .

4.5 The C IV line as a black hole mass estimator

As can be seen in Fig. 8 and also mentioned in Section 4.3, the width of C IV shows only weak correlations (if at all) with the widths of the other lines we study in this paper. This result together with the significant blueshifts observed in the C IV line centre ($\Delta v = -1200 \pm 1000$) make mass estimates based on the C IV line significantly more uncertain. However, in high- z objects ($2 \lesssim z \lesssim 5$) C IV is the only prominent broad emission line that lies within the optical window. It is therefore important to explore possibilities to improve M_{BH} determination by means of C IV . There have been already some attempts in this direction. For instance, R13 and Brotherton et al. (2015) claim a correlation between the line peak ratio $L_{\text{P}}(\text{Si IV} + \text{O IV})/L_{\text{P}}(\text{C IV})$ and the FWHM ratio $\text{FWHM}(\text{C IV})/\text{FWHM}(\text{H}\beta)$ driven by eigenvector 1 (Boroson & Green 1992) that would help to reduce the scatter in M_{BH} from 0.43 to 0.30 dex; D13 propose that having high-quality spectra and using the velocity dispersion of the line (σ_{line}), instead of FWHM, will lead to accurate M_{BH} estimations. However, D13 sample is limited to only six objects and our larger, high-quality sample does not show any correlation between $\sigma_{\text{line}}(\text{H}\beta)$ and $\sigma_{\text{line}}(\text{C IV})$.

In the following section, we test the R13 suggested relation as well as other relationships that can be used to improve the C IV -based mass determination method.

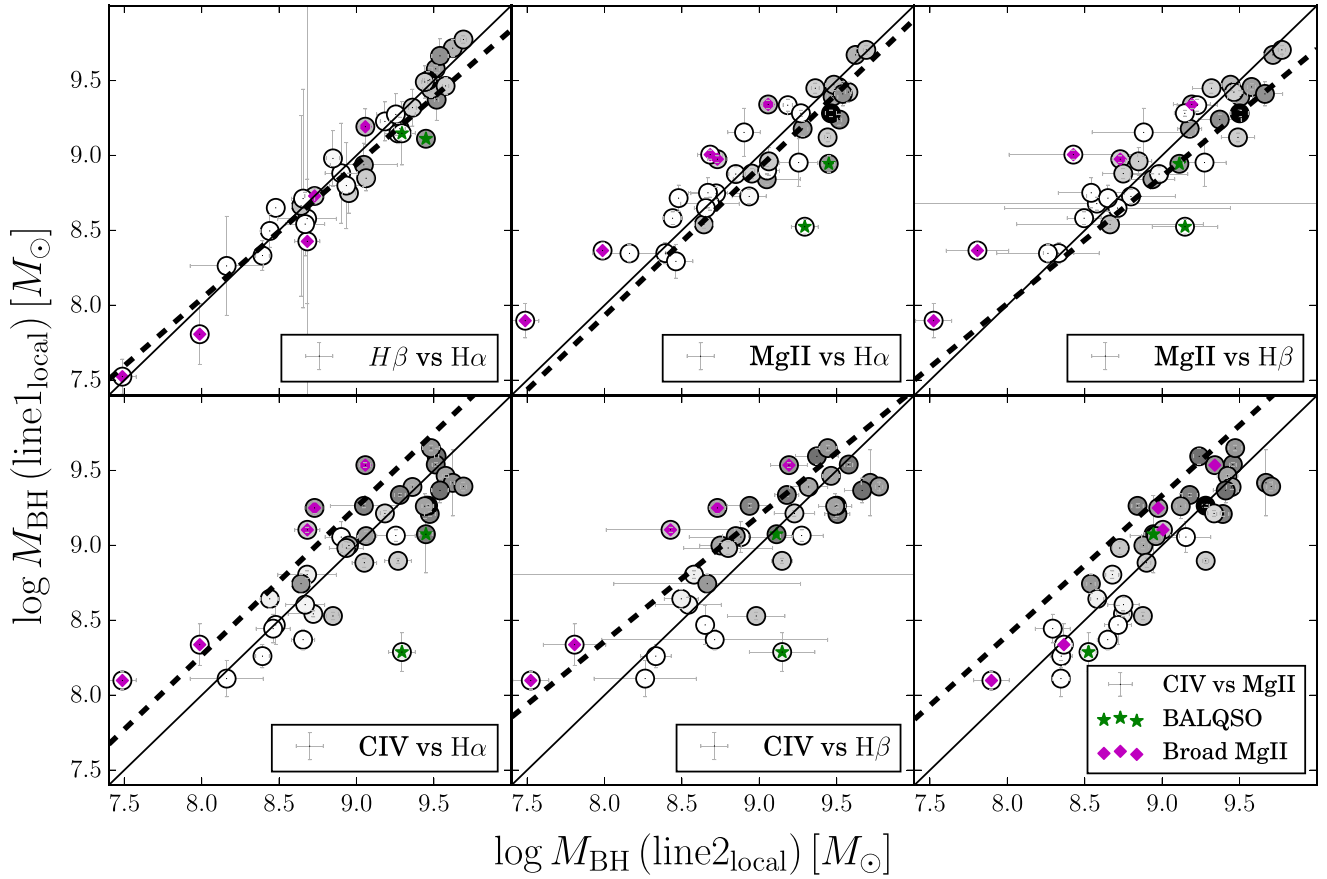


Figure 9. Comparisons between different M_{BH} estimates that are derived from different lines as indicated in the inserts of each panel. The black solid line represents the 1:1 relation. $H\alpha$ values were derived using L_{6200} . The dashed black line represents the best fit to previous black hole mass estimators. Points are colour-coded in grey-scale by the S/N of the continuum bands around $H\beta$ where darker colours translates into larger S/N. BALQSO and the broad-Mg II objects (see Section 4.3.4) are the labelled by green stars and magenta diamonds, respectively.

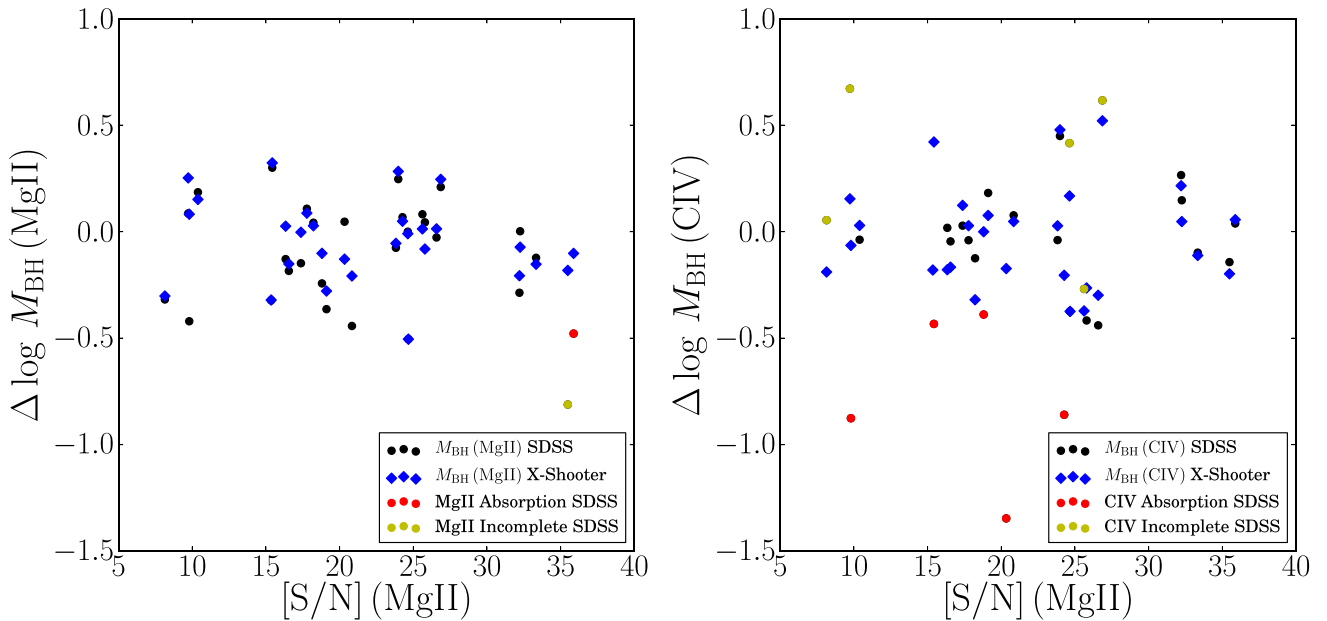


Figure 10. A comparison of M_{BH} estimates from X-Shooter and SDSS spectra. We show the offsets in mass estimates, $\Delta \log M_{\text{BH}} \equiv \log(M_{\text{BH}}(\text{line})/M_{\text{BH}}(H\alpha))$, versus the S/N of the continuum around Mg II ($[S/N](\text{Mg II})$) using SDSS (black dots) and X-Shooter (blue diamonds) data for the Mg II (left panel) and CIV (right panel) lines. SDSS data with unresolved absorption features (red dots) or incomplete line profiles (yellow dots) are also shown.

Table 8. Spearman correlation coefficients, probability, scatter and the best-fitting parameters ($\log \text{FWHM}_{\text{ratio}} = \beta \log L_{\text{P}}^{\text{ratio}} + C$) between the listed quantities.

	— $\log(L_{\text{P}}(\text{Si IV} + \text{O IV})/\lambda 1400)/L_{\text{P}}(\text{C IV})$ —					— $\log(L_{\text{P}}(\text{C III}]\lambda 1909)/L_{\text{P}}(\text{C IV}))$ —				
	r_s	P	Scatter(dex)	β	C	r_s	P (per cent)	Scatter (dex)	β	C
$\log(\text{FWHM}(\text{C IV})/\text{FWHM}(\text{H}\alpha))$	0.36	0.02	0.35	0.76	−0.51	0.34	3	0.34	0.72	−0.55
$\log(\text{FWHM}(\text{C IV})/\text{FWHM}(\text{H}\beta))$	0.44	0.003	0.32	0.55	−0.31	0.47	0.2	0.30	0.57	−0.33
$\log(\text{FWHM}(\text{C IV})/\text{FWHM}(\text{Mg II}))$	0.51	0.003	0.28	0.69	−0.72	0.57	0.02	0.19	0.52	−0.52
$\log(\text{FWHM}(\text{C IV})/\text{FWHM}(\text{H}\beta))$ from R13	0.64	3×10^{-9}	0.26	0.57	−0.36	–	–	–	–	–

4.5.1 Rehabilitating C IV?

In Table 8, we show the correlation coefficient, correlation probability and scatter between $L_{\text{P}}(\text{Si IV} + \text{O IV})/L_{\text{P}}(\text{C IV})$ and $\text{FWHM}(\text{C IV})/\text{FWHM}(\text{H}\beta)$ as well as several other similar line peak and FWHM ratios that are listed in the table. In Fig. 11, we compare such quantities.

As can be seen in Table 8 and Fig. 11, we confirm the correlation reported by R13, however with a lower level of significance and larger scatter. These differences may be attributed to the smaller size of our sample (39 objects here versus 85 in R13), and the somewhat lower S/N in the H β region for the fainter sources in our sample, compared with R13. We can also see in Table 8 and Fig. 11 that our best-fitting relation between $L_{\text{P}}(\text{Si IV} + \text{O IV})/L_{\text{P}}(\text{C IV})$ and $\text{FWHM}(\text{C IV})/\text{FWHM}(\text{H}\beta)$ (black solid line in the top-middle panel) is in very good agreement with the one presented in R13 (red dashed line in the top-middle panel).

We also find that $L_{\text{P}}(\text{C III}]/L_{\text{P}}(\text{C IV})$ correlations are slightly stronger than the analogous $L_{\text{P}}(\text{Si IV} + \text{O IV})/L_{\text{P}}(\text{C IV})$ correlations. At the same time, the strongest correlations are those involving these line peak ratios and $\text{FWHM}(\text{C IV})/\text{FWHM}(\text{Mg II})$. These relationships can be used to derive ‘corrected’ M_{BH} estimates in cases where the relevant line peak ratios can be observed.

Below we present the corrected M_{BH} that can be derived from C IV and Si IV+O IV] measurements:

$$M_{\text{BH}}(\text{Mg II})_{\text{pred}} = 1.13 \times 10^6 \left(\frac{L_{1450}}{10^{44}} \right)^{0.57} \times \left(\frac{\text{FWHM}(\text{C IV})}{10^3 \text{ km s}^{-1}} \right)^2 \times \left(\frac{L_{\text{P}}(\text{Si IV} + \text{O IV])}{L_{\text{P}}(\text{C IV})} \right)^{-1.66} \quad (6)$$

and from C IV and C III] measurements:

$$M_{\text{BH}}(\text{Mg II})_{\text{pred}} = 5.71 \times 10^5 \left(\frac{L_{1450}}{10^{44} \text{ erg s}^{-1}} \right)^{0.57} \times \left(\frac{\text{FWHM}(\text{C IV})}{10^3 \text{ km s}^{-1}} \right)^2 \times \left(\frac{L_{\text{P}}(\text{C III])}}{L_{\text{P}}(\text{C IV})} \right)^{-2.09} \quad (7)$$

The confirmation of the R13 correlation, and the new correlations reported here, should assist in rehabilitating C IV for more reliable M_{BH} measurements, by relying on the nearby Si IV+O IV] and/or C III] emission lines. Even for those combinations of observables which do not significantly reduce the scatter in M_{BH} determinations, they provide an improvement in the *accuracy* of rest-frame UV-based M_{BH} estimations since these prescriptions compensates the effect of L/L_{Edd} in the C IV profile.

5 SUMMARY AND CONCLUSIONS

This paper uses a unique sample of 39 type I AGN observed by X-Shooter and covering, uniformly, the $M_{\text{BH}}-L/L_{\text{Edd}}$ plane at $z = 1.55$ down to $i_{\text{AB}} \sim 21$ mag. Our sample allows for a comprehensive

comparison between different luminosity probes and emission line measurements, for the prominent broad emission lines H α , H β , Mg II and C IV, which are commonly used for virial BH mass estimates. Thanks to the broad spectral coverage we were also able to test two approaches for continuum fitting and test for possible biases in M_{BH} determinations: a physically motivated approach based on fitting an AD model to each spectrum; and a more practical approach which treats the continuum around each prominent line as an independent power law.

In summary, the main findings of this work are as follows.

(i) Comparing the two continuum fitting approaches, we find only small (although systemic) offsets in the derived line luminosities, local continua luminosities and line FWHMs, and consequently in M_{BH} determinations (<0.05 dex). This implies that a precise modelling of the continuum emission is *not* crucial for M_{BH} determinations.

(ii) Line dispersion measurements (σ_{line}) are highly sensitive to continuum modelling, and cannot be safely used for M_{BH} determination, even for the well-studied Balmer lines and/or when high-quality spectra of broad UV lines are available.

(iii) We corroborate that both the H α and H β lines show very similar FWHMs and can be consistently used for estimating M_{BH} based on the virial assumption.

(iv) The Mg II line width is found to follow that of H β , and, generally, can be safely used for M_{BH} estimations. Our new observations show that the Mg II line is about 30 ± 15 per cent narrower than H β (in FWHM). We also found that about 10 per cent of the objects show atypically *broad* Mg II lines, with $\text{FWHM}(\text{Mg II}) \gtrsim \text{FWHM}(\text{H}\alpha)$. These Mg II profiles are also systematically blueshifted, probably due to non-virial dynamics, and further shown to be not suitable for reliable M_{BH} estimation (see Section 4.3.4). We note that broad-Mg II objects can only be identified using additional information from one of the Balmer lines, which would in turn eliminate the necessity to identify them. Without any additional information, such sources may be present in any sample of AGN.

(v) We find that FWHM measurements for C IV in low-S/N spectra are systematically underestimated, for objects with partially resolved or unresolved C IV absorption features. We also find and that the FWHMs of Mg II and the FWHMs of non-absorbed-C IV-profiles are consistent in low- and high-S/N data sets. On the other hand, the line dispersion measurements (σ_{line}) for both C IV and Mg II profiles differ significantly (a scatter of ~ 0.2 dex).

(vi) We find better agreement and lower dispersion between L_{6200} and L_{5100} than between $L(\text{H}\alpha)$ and L_{5100} , especially for high-luminosity objects ($L_{5100} > 10^{45} \text{ erg s}^{-1}$), and recommend to use the L_{6200} -FWHM(H α) black hole mass calibration (Table 7) for objects with an AGN-dominated continuum in this luminosity range.

(vii) The considerable uncertainties associated with C IV-based determination of M_{BH} are not solely due to insufficient spectral resolution and/or S/N. They are more likely related to the physics of the

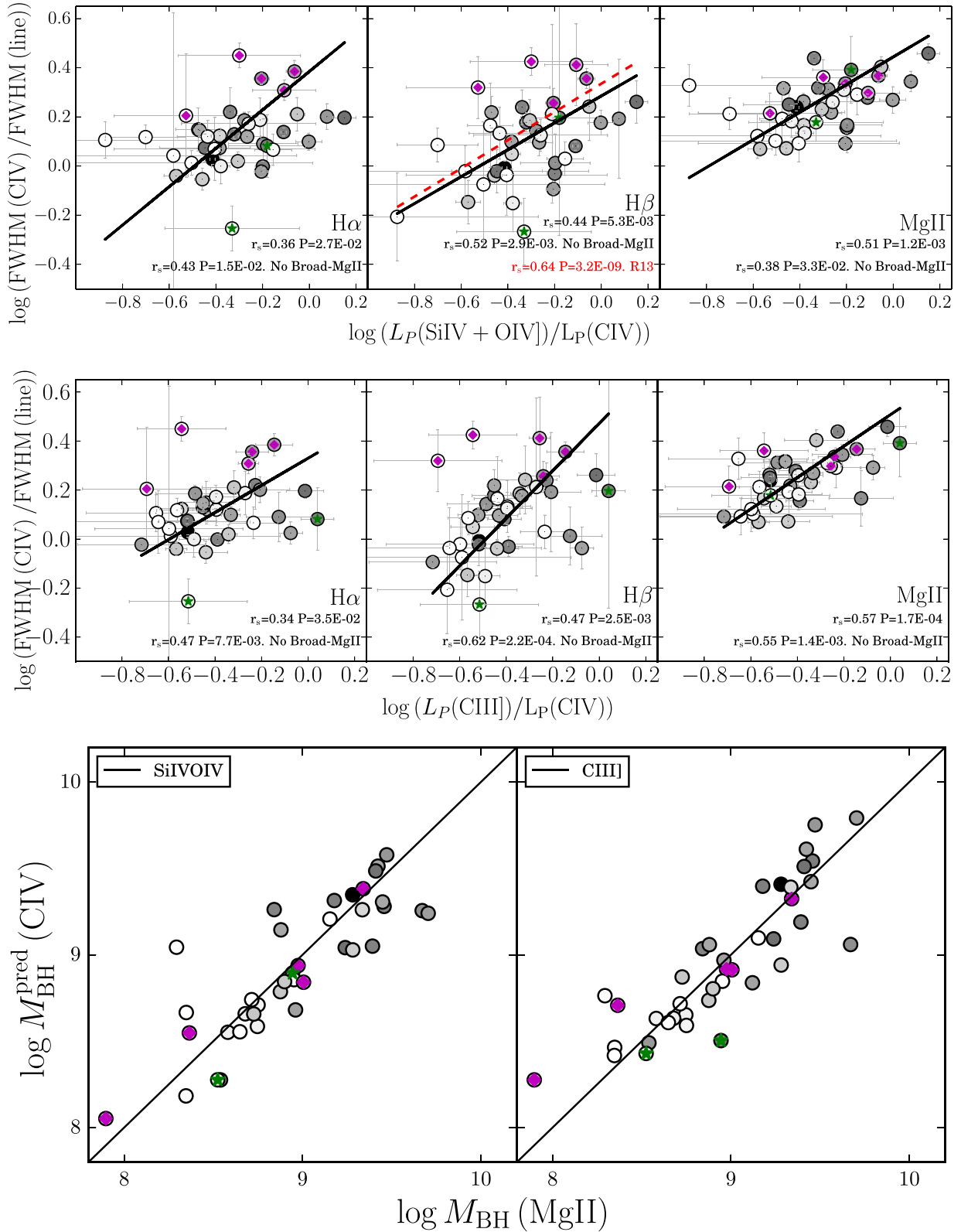


Figure 11. Top panel: comparison of the H α -CIV (left), H β -CIV (middle) and MgII-CIV (right) FWHM ratios with the SiIV+OIV-CIV line peak ratio. The red dashed line represents the best-fitting relation reported by R13, and the black solid lines represent our best-fitting relation. Middle panel: same as the top panel but this time we compare with the CIII]-CIV line peak ratio. Bottom panel: predicted M_{BH} masses using the correlations of the MgII-CIV FWHM ratio with the SiIV+OIV-CIV (bottom left) and the CIII]-CIV (bottom right) line peak ratios. Green stars represent broad absorption lines quasars (BALQSO) and magenta points represent the broad-MgII objects. The black solid lines represent the 1:1 relation.

BLR. Our results are in agreement with some earlier findings about the systematic uncertainties associated with C_{IV} . We found that the L/L_{Edd} is strongly correlated with $FWHM(C_{IV})/FWHM(H\alpha)$ and with the velocity offset of the C_{IV} line. We stress, however, that these correlations show large scatter and cannot practically assist in improving $M_{BH}(C_{IV})$ estimates.

(viii) We confirm the result of R13, finding a significant correlation between the $Si_{IV}+O_{IV}/C_{IV}$ line peak ratio and $FWHM(C_{IV})/FWHM(H\beta)$, which may in principle assist rehabilitating C_{IV} -based M_{BH} determinations. Moreover, we find even stronger correlations associated with the C_{III}/C_{IV} line peak ratio. Although these empirical correlations do *not* significantly reduce the scatter in $M_{BH}(C_{IV})$ estimates, we propose that their application, whenever possible, would improve the accuracy of C_{IV} -based M_{BH} determinations.

(ix) L/L_{Edd} seems to affect the dynamics of the Mg_{II} -emitting region, especially in objects with extreme accretion rates (as pointed out by M13).

(x) We provide new single-epoch calibrations for M_{BH} , based on the FWHM of $H\alpha$, $H\beta$, Mg_{II} and C_{IV} .

(xi) We constructed a new (UV) iron template that aims to improve on previous templates (Vestergaard & Wilkes 2001; T06), particularly in the region of $\sim 2200\text{--}3650 \text{ \AA}$.

ACKNOWLEDGEMENTS

We thank the anonymous referee for the detailed and constructive feedback, which helped us in improving the paper. JM acknowledges ‘CONICYT-PCHA/doctorado Nacional para extranjeros/2013-63130316’ for their PhD scholarship support, Fondecyt Project #1120328 for their support in computing facilities and travel to Tel Aviv University, where an important part of the work was done. JM is also grateful for the hospitality and support of Tel Aviv university during two visits. Funding for this work has been provided by the Israel Science Foundation grant 284/13.

REFERENCES

Abazajian K. N. et al., 2009, *ApJS*, 182, 543
 Baskin A., Laor A., 2005, *MNRAS*, 356, 1029
 Bentz M. C., Peterson B. M., Netzer H., Pogge R. W., Vestergaard M., 2009, *ApJ*, 697, 160
 Bentz M. C. et al., 2013, *ApJ*, 767, 149
 Boroson T. A., Green R. F., 1992, *ApJS*, 80, 109
 Brotherton M. S., Singh V., Runnoe J., 2015, *MNRAS*, 454, 3864
 Brotherton M. S., Runnoe J. C., Shang Z., DiPompeo M. A., 2015, *MNRAS*, 451, 1290
 Capellupo D. M., Netzer H., Lira P., Trakhtenbrot B., Mejía-Restrepo J., 2015, *MNRAS*, 446, 3427 (Paper I)
 Capellupo D. M. et al., 2016, *MNRAS*, 460, 212 (Paper III)
 Corbin M. R., 1990, *ApJ*, 357, 346
 Corbin M. R., Boroson T. A., 1996, *ApJS*, 107, 69
 Croom S. M., Smith R. J., Boyle B. J., Shanks T., Miller L., Outram P. J., Loaring N. S., 2004, *MNRAS*, 349, 1397
 Denney K. D., 2012, *ApJ*, 759, 44
 Denney K. D., Peterson B. M., Dietrich M., Vestergaard M., Bentz M. C., 2009, *ApJ*, 692, 246
 Denney K. D., Pogge R. W., Assef R. J., Kochanek C. S., Peterson B. M., Vestergaard M., 2013, *ApJ*, 775, 60 (D13)
 Ferrarese L., Merritt D., 2000, *ApJ*, 539, L9
 Fine S. et al., 2006, *MNRAS*, 373, 613
 Fine S. et al., 2008, *MNRAS*, 390, 1413
 Fine S., Croom S. M., Bland-Hawthorn J., Pimblet K. A., Ross N. P., Schneider D. P., Shanks T., 2010, *MNRAS*, 409, 591
 Gaskell C. M., 1982, *ApJ*, 263, 79

Gaskell C. M., 2009, *New Astron. Rev.*, 53, 140
 Gaskell C. M., Goosmann R. W., 2013, *ApJ*, 769, 30
 Ginsburg A., Mirocha J., 2011, *Astrophysics Source Code Library*, record ascl:1109.001
 Goosmann R. W., Gaskell C. M., 2007, *A&A*, 465, 129
 Graham A. W., 2016, *ASSL*, 418, 263
 Graham A. W., Onken C. A., Athanassoula E., Combes F., 2011, *MNRAS*, 412, 2211
 Grandi S. A., 1982, *ApJ*, 255, 25
 Greene J. E., Ho L. C., 2005, *ApJ*, 630, 122
 Gültekin K. et al., 2009, *ApJ*, 698, 198
 Häring N., Rix H.-W., 2004, *ApJ*, 604, L89
 Hewett P. C., Wild V., 2010, *MNRAS*, 405, 2302
 Ho L. C., Goldoni P., Dong X.-B., Greene J. E., Ponti G., 2012, *ApJ*, 754, 11
 Kallman T. R., Krolik J. H., 1986, *ApJ*, 308, 805
 Kaspi S., Smith P. S., Netzer H., Maoz D., Jannuzi B. T., Giveon U., 2000, *ApJ*, 533, 631
 Kaspi S., Maoz D., Netzer H., Peterson B. M., Vestergaard M., Jannuzi B. T., 2005, *ApJ*, 629, 61
 Kaspi S., Brandt W. N., Maoz D., Netzer H., Schneider D. P., Shemmer O., 2007, *ApJ*, 659, 997
 Laor A., Jannuzi B. T., Green R. F., Boroson T. A., 1997, *ApJ*, 489, 656
 Marziani P., Dultzin-Hacyan D., Sulentic J. W., 2006, in Kreidler P. V., ed., *Accretion onto Supermassive Black Holes in Quasars: Learning from Optical/UV Observations*. Nova Science Publishers, New York, p. 123
 Marziani P., Sulentic J. W., Plauchu-Frayn I., del Olmo A., 2013a, *A&A*, 555, A89 (M13)
 Marziani P., Sulentic J. W., Plauchu-Frayn I., del Olmo A., 2013b, *ApJ*, 764, 150
 McLure R. J., Dunlop J. S., 2004, *MNRAS*, 352, 1390
 McLure R. J., Jarvis M. J., 2002, *MNRAS*, 337, 109
 Müller A., Wold M., 2006, *A&A*, 457, 485
 Netzer H., 1977, *MNRAS*, 181, 89p
 Netzer H., 2006, *ApJ*, 652, L117
 Netzer H., Lira P., Trakhtenbrot B., Shemmer O., Cury I., 2007, *ApJ*, 671, 1256
 Onken C. A., Ferrarese L., Merritt D., Peterson B. M., Pogge R. W., Vestergaard M., Wandel A., 2004, *ApJ*, 615, 645
 Park D., Woo J.-H., Denney K. D., Shin J., 2013, *ApJ*, 770, 87
 Peterson B. M., Wandel A., 1999, *ApJ*, 521, L95
 Peterson B. M. et al., 2004, *ApJ*, 613, 682
 Popovic L. C., Vince I., Atanackovic-Vukmanovic O., Kubicela A., 1995, *A&A*, 293, 309
 Rafiee A., Hall P. B., 2011, *ApJS*, 194, 42
 Richards G. T., Vanden Berk D. E., Reichard T. A., Hall P. B., Schneider D. P., SubbaRao M., Thakar A. R., York D. G., 2002, *AJ*, 124, 1
 Richards G. T. et al., 2011, *AJ*, 141, 167
 Runnoe J. C., Brotherton M. S., Shang Z., DiPompeo M. A., 2013, *MNRAS*, 434, 848 (R13)
 Runnoe J. C., Brotherton M. S., DiPompeo M. A., Shang Z., 2014, *MNRAS*, 438, 3263
 Shakura N. I., Sunyaev R. A., 1973, *A&A*, 24, 337 (SS73)
 Shang Z., Wills B. J., Wills D., Brotherton M. S., 2007, *AJ*, 134, 294 (S07)
 Shen Y., 2013, *Bull. Astron. Soc. India*, 41, 61
 Shen Y., Ho L. C., 2014, *Nature*, 513, 210
 Shen Y., Liu X., 2012, *ApJ*, 753, 125
 Shen Y., Greene J. E., Strauss M. A., Richards G. T., Schneider D. P., 2008, *ApJ*, 680, 169
 Slone O., Netzer H., 2012, *MNRAS*, 426, 656
 Sulentic J. W., Marziani P., Zamanov R., Bachev R., Calvani M., Dultzin-Hacyan D., 2002, *ApJ*, 566, L71
 Sulentic J. W., Bachev R., Marziani P., Negrete C. A., Dultzin D., 2007, *ApJ*, 666, 757
 Tilton E. M., Shull J. M., 2013, *ApJ*, 774, 67
 Trakhtenbrot B., Netzer H., 2012, *MNRAS*, 427, 3081 (TN12)
 Trakhtenbrot B., Netzer H., Lira P., Shemmer O., 2011, *ApJ*, 730, 7
 Tremaine S., Shen Y., Liu X., Loeb A., 2014, *ApJ*, 794, 49

- Tsuzuki Y., Kawara K., Yoshii Y., Oyabu S., Tanabé T., Matsuoka Y., 2006, ApJ, 650, 57 (T06)
- Vanden Berk D. E. et al., 2004, ApJ, 601, 692
- Vestergaard M., 2002, ApJ, 571, 733
- Vestergaard M., Osmer P. S., 2009, ApJ, 699, 800
- Vestergaard M., Peterson B. M., 2006, ApJ, 641, 689
- Vestergaard M., Wilkes B. J., 2001, ApJS, 134, 1 (VW01)
- Wang J.-G. et al., 2009, ApJ, 707, 1334
- Wills B. J., Netzer H., Brotherton M. S., Han M., Wills D., Baldwin J. A., Ferland G. J., Browne I. W. A., 1993, ApJ, 410, 534
- Woo J.-H. et al., 2010, ApJ, 716, 269
- Woo J.-H., Yoon Y., Park S., Park D., Kim S. C., 2015, ApJ, 801, 38
- Xiao T., Barth A. J., Greene J. E., Ho L. C., Bentz M. C., Ludwig R. R., Jiang Y., 2011, ApJ, 739, 28
- Zheng W., Sulentic J. W., 1990, ApJ, 350, 512
- Zuo W., Wu X.-B., Fan X., Green R., Wang R., Bian F., 2015, ApJ, 802, 140

APPENDIX A: DEMONSTRATING THE QUALITY OF X-SHOOTER SPECTRA

Fig. A1 compares the newly obtained X-Shooter spectrum (UVB+VIS arms) to the publicly available SDSS spectrum, for

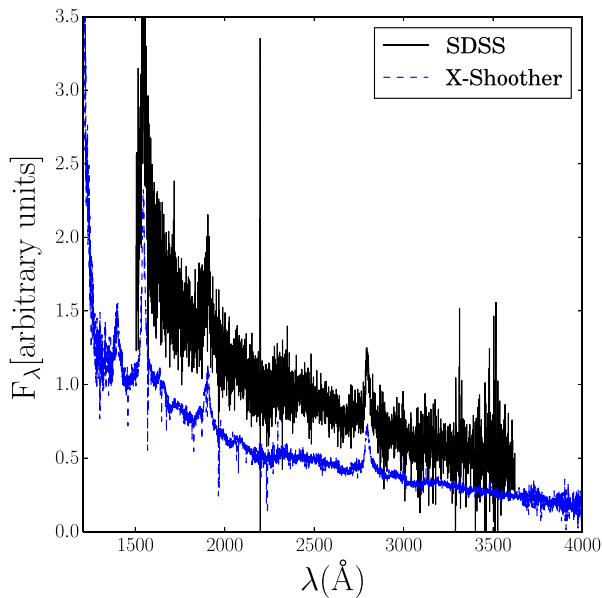


Figure A1. SDSS and X-Shooter spectra of J0143–0056. Both spectra have been re-scaled to avoid overlapping.

J0143–0056 - the source shown in Figs 3 and 4. This source has an S/N $\simeq 25$ at 2000 Å which lies in the middle of the S/N range for the entire sample. Both spectra are presented *without* any binning or smoothing, including the residual sky and/or instrumental features. We note the significant improvements to S/N and spectral resolution, as evident from the minor absorption feature on the blue wing of the C III] $\lambda 1909$ line. The broader spectral coverage allows for a much more robust determination of the continuum level next to the C IV and Mg II emission lines (i.e. L_{1450} and L_{3000}). Obviously, the NIR arm of X-Shooter includes the H β and H α spectral regions (not shown here), which are unavailable in the SDSS data.

APPENDIX B: NEW UV IRON EMISSION TEMPLATE

In Fig. B1, we compare our new UV iron template with the template of T06. The new template, covering 2200–3646 Å and with an intrinsic width of 900 km s $^{-1}$, can be downloaded from http://www.das.uchile.cl/jemejia/feII_UV_Mejia-Restrepo_et_al_2015_2200-3646AA.data.

We prefer the use of our new template motivated by the following three reasons.

(i) The T06 template severely underestimates the continuum emission around 2100 Å.

(ii) T06 modelled the BC continuum as a modified black body following Grandi (1982). This does not provide a good approximation to Balmer emission and we prefer templates based on photoionization calculations.

(iii) The T06 template only extends between 2200 and 3500 Å. However, there is still a remaining weaker but still non-negligible contribution from iron emission up to the Balmer limit (3647 Å). The correct estimation of iron emission in this regions (3500–3647 Å) is crucial for estimating the emission by iron lines and to prevent overestimation of the BC.

We constructed the template following T06 and VW01 procedures and using our own estimations of the AD emission and Balmer continua. We redefined the AD continuum by manually selecting the continuum windows at ~ 2100 and ~ 4200 Å which account for the region where we require to obtain the new iron template (2100–3647 Å). The BC model that we use is described in Section 3.

Our template provides stronger iron emission, particularly in the range of 2620–3500 Å, which is crucial for Mg II measurements.

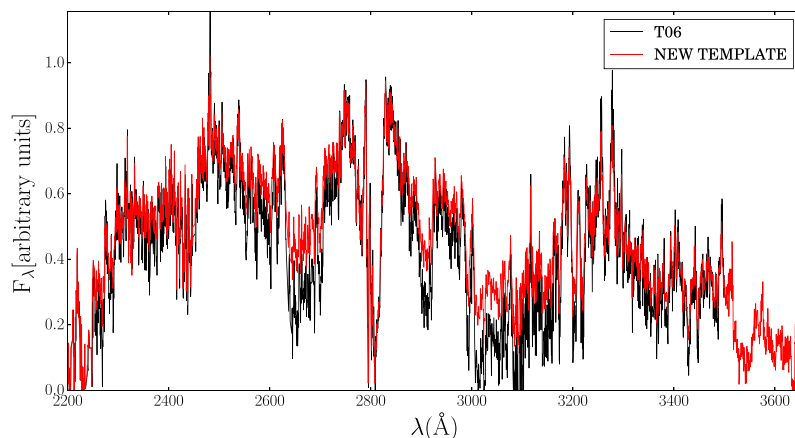


Figure B1. Comparison of our new template (red) and T06 template (black).

This could be explained by our different BC approach and disc continuum windows.

APPENDIX C: COMPARISON OF OBSERVED EMISSION LINE PROFILES

In Figs C1 and C2, we show the normalized profiles of the $H\alpha$, $H\beta$, $Mg\text{II}$ and $C\text{IV}$ emission lines, in velocity space. In most but not all sources, the $C\text{IV}$ profiles (red) are broader and blueshifted

with respect to the $H\alpha$ and $H\beta$ line profiles as discussed in Section 4.3. The low-ionization lines, $H\alpha$, $H\beta$ and $Mg\text{II}$, show similar shape profiles. $H\beta$ is generally slightly broader than $H\alpha$. $Mg\text{II}$ is, on average, 30 per cent narrower than $H\beta$. The five broad- $Mg\text{II}$ objects (top row) show $Mg\text{II}$ that are broader than $H\alpha$ and $H\beta$. These $Mg\text{II}$ profiles are also slightly blueshifted (about 300 km s^{-1}) relative to the $H\beta$ line. The two BALQSOs are the last two objects of the bottom row on the second set.

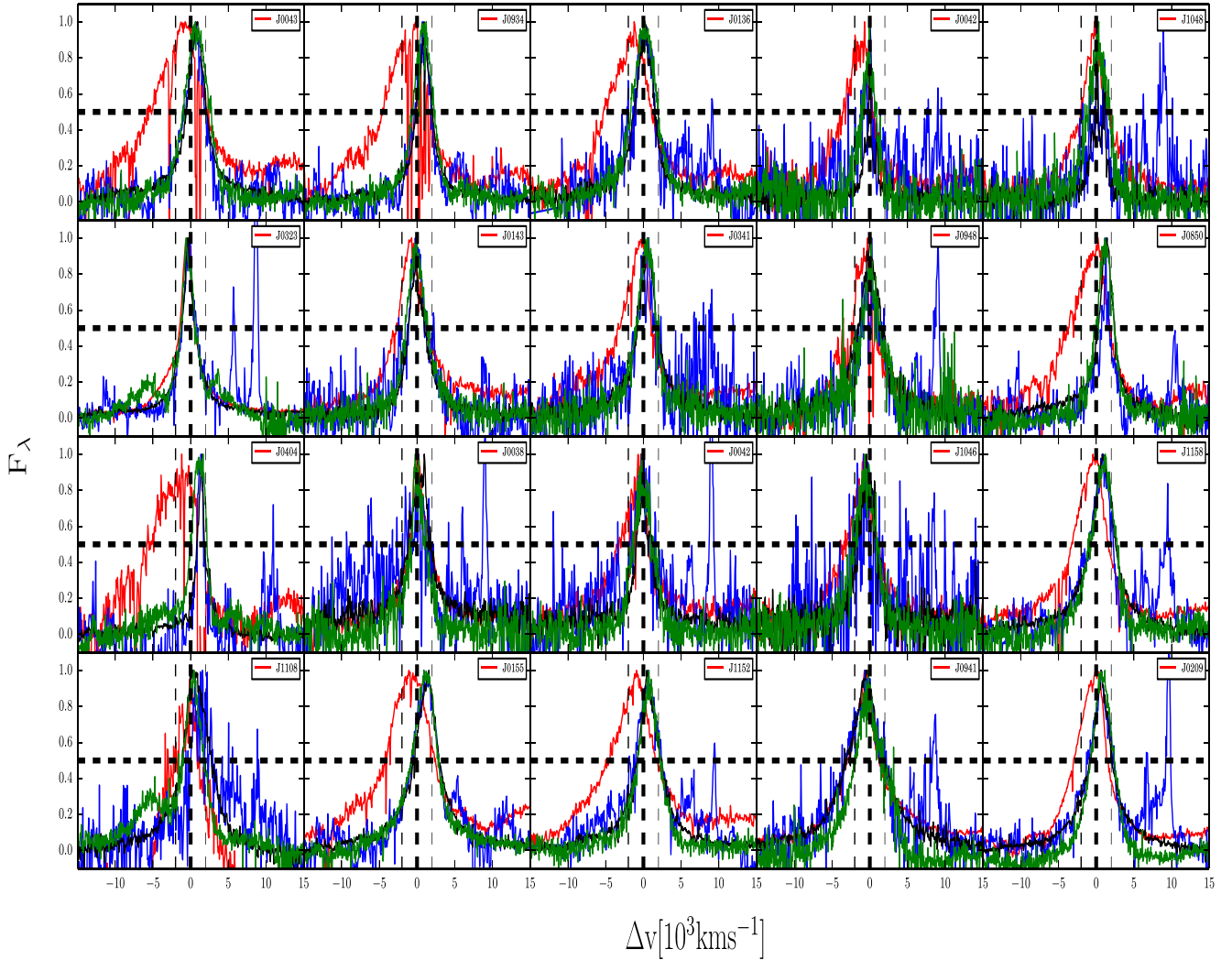


Figure C1. Comparison of the observed $H\alpha$ (black), $H\beta$ (blue), $Mg\text{II}$ (green) and $C\text{IV}$ (red) line profiles in the velocity space for the objects in the sample with satisfactory thin disc continuum fits. All profiles have been normalized relative to the peak flux density of the line. It is important to remark that both the $Mg\text{II}$ and $C\text{IV}$ profiles are doublets and their decomposed profiles are narrower than shown here. In the top row we show the five broad- $Mg\text{II}$ objects.

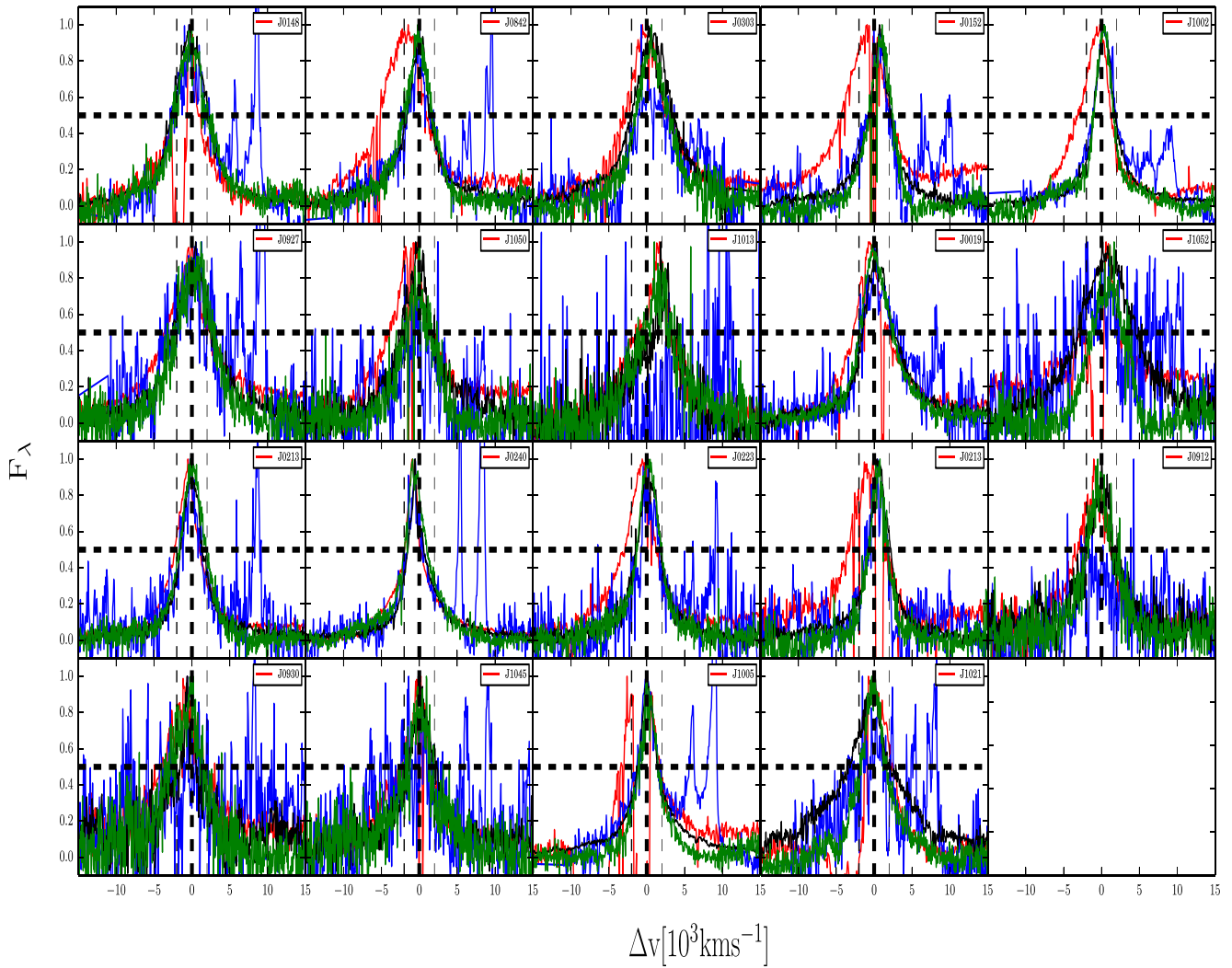


Figure C2. Continued from Fig. C1. Comparison of the observed H α (black), H β (blue), Mg II (green) and C IV (red) line profiles in the velocity space for the objects in the sample with satisfactory thin disc continuum fits. All profiles have been normalized relative to the peak flux density of the line. It is important to remark that both the Mg II and C IV profiles are doublets and their decomposed profiles are narrower than shown here. To the left of the bottom row we show the two BALQSO objects.

APPENDIX D: EMISSION LINE CONSTRAINTS

Table D1 lists the constraints on the emission line modelling for each of the components in our fitting procedure following Shang et al. (2007) and Vanden Berk et al. (2004).

Table D1. Line regions and adopted constraints. Under the *global* approach the C IV and C III] line regions are fitted simultaneously.

ID	LINE	λ	GAUSSIAN COMPONENT	Flux	Center	FWHM	FLUX RATIO
Si IV + O IV] Region							
1	Si IV	1396.75	Broad	Free	Free	Free	Free
2			Narrow	Free	1	Free	Free
3	O IV]	1402.34	Broad	Free	1	Free	Free
4			Narrow	Free	2	Free	Free
C IV Region							
1	N IV]	1486.5		Free	Free	Free	
2	C IV	1548.2	Narrow	Free	Free	Free	Free
3			Broad	Free	Free	Free	Free
4	C IV	1550.77	Narrow	Free	2	2	1
5			Broad	Free	3	3	1
6	He II	1640.72	Narrow	Free	Free	Free	
7			Broad	Free	6	Free	
8	O III]	1660.8		Free	1	Free	0.29
9		1666.14		8	8	8	0.71
10	N IV	1718.75		Free	Free	Free	Free
C III] Region							
11	C III]	1908.73	Narrow	Free	Free	Free	
12			Broad	Free	13	Free	
13	Si III]	1892.03		Free	11	Free	
14	Al III]	1854.72		Free	13	Free	1
15		1862.78		14	14	14	1
16	Si II	1818.17		Free	11	Free	
17	Fe II	1788.73		16	16	16	
18	N III]	1748.65		13	13	13	0.41
19		1752.16		18	18	18	0.14
20		1754.00		18	18	18	0.45
Mg II Region							
1	Mg II	2795.53	Narrow	Free	Free	Free	2
2			Broad	Free	1	Free	2
3	Mg II	2802.71	Narrow	1	1	1	1
4			Broad	2	2	2	1
5	Fe	Template		Free	Free	Free	
H β Region							
1	H β	4861.32	Narrow	Free	Free	Free	
2			Broad	Free	Free	Free	
3			NLR	Free	4	4	
4	[O III]	5006.84		Free	Free	Free	3
5		4958.91		4	4	4	1
6	He II	4685.65		Free	Free	Free	
7	Fe II	s		Free	–	Free	
H α Region							
1	H α	6562.8	Narrow	Free	Free	Free	
2			Broad	Free	Free	Free	
3			NLR	Free	Free	4	
4	[N II]	6548.06		Free	4	[O III] width	1
5		6583.39		4	4	4	3
6	[S II]	6716.47		Free	4	4	1
7		6730.85		6	6	6	1

This paper has been typeset from a $\text{\TeX}/\text{\LaTeX}$ file prepared by the author.